3D microstructure modelling of coating layers including grain boundaries

Bachelor's thesis

Degree Programme in Mechanical Engineering and Production Technology

Rihimäki, BEMPNU13A6

Ivan Yashchuk

Riihimäki
Degree Programme in Mechanical Engineering and Production Technology

Author Ivan Yashchuk **Year** 2016

Subject of Bachelor's thesis 3D microstructure modelling of coating layers including grain boundaries.

ABSTRACT

Nowadays, coatings have a significant role in increasing the lifetime of manufactured products. A coating layer applied to the surface of a product increases its corrosion and wear resistance. As with any other materials, coatings are subjected to damage phenomena. The damage of the coating layer usually happens because of delamination and crack propagation inside the coating layer. In order to know how to improve the coating resistance the fracture behavior is studied using finite element analysis. The system under analysis consists of two parts: the coating layer and the substrate.

The Cohesive Zone Modelling technique is used to predict and describe the damage initialization and propagation. The delamination behavior is described with the cohesive elements between the coating and the substrate. Inside the coating layer, the crack usually propagates between the grains of the material. Therefore, to capture an intergranular fracture behavior first a microstructure model of the coating layer is generated, then cohesive elements are placed between the grains of the coating. For this purpose, a mathematical tool called the Voronoi diagram, which mimics the grain structure of materials, is implemented in the MATLAB script.

Tensile tests and nanoindentation tests were performed in this project to validate the coating-substrate model with cohesive zone elements.

The results showed that it is possible to vary the morphology of the microstructure and to change the damage behavior in the coating. The developed scripts could be used to obtain quantitatively accurate results of the coating microstructure response under loads.

Keywords Voronoi diagram, microstructure, cohesive zone elements.

Pages 35 p.

LIST OF ABREVIATIONS AND SYMBOLS

HPPMS	High Power Pulsed Magnetron Sputtering
CZM	Cohesive Zone Modelling
TSL	Traction Separation law
R_i	the i-th Voronoi region
P_i	the i-th seed point
P	the set of points
$DT(P)$	the Delaunay triangulation of P
Nx	the number of grid regions in x-direction
Ny	the number of grid regions in y-direction
Nz	the number of grid regions in z-direction
Lx	the length of the specimen domain in x-direction
Ly	the length of the specimen domain in y-direction
Lz	the length of the specimen domain in z-direction
$\boldsymbol{t}$	the traction stress vector
t_n	the normal component of the traction stress vector
t_{s1}, t_{s2}	the tangential components of the traction stress vector
$\boldsymbol{\delta}$	the separation vector
δ_n	the normal component of the separation vector
δ_{s1}, δ_{s2}	the tangential component of the separation vector
$\boldsymbol{K}$	the stiffness matrix
β	the ratio of shear to normal cohesive strengths
$\langle\,\rangle$	the Macaulay brackets
D	the damage variable
λ	the effective separation
λ_0	the effective separation at damage initiation point
λ_f	the effective separation at failure point
$\boldsymbol{t}_D$	the traction separation vector after the damage initiation
W_{int}	the internal work
$\boldsymbol{E}$	the Green strain tensor
Ω	the domain
$\delta\boldsymbol{u}$	the virtual displacement
Γ	the boundary
$\boldsymbol{T}_{ext}$	the external traction
$\boldsymbol{S}$	the second Piola-Kircchoff stress tensor
W_{ext}	the external work
$\boldsymbol{T}_c$	the cohesive traction
Γ_c	the fracture surface
$\delta\boldsymbol{\Delta}$	the virtual separation
ξ, η	the local coordinates
$\boldsymbol{B}$	the global displacement-separation marix
$\boldsymbol{\Theta}$	the transformation vector
$\boldsymbol{K}_{local}$	the local stiffness matrix
$\boldsymbol{t}_{local}$	the local traction vector
$\det\boldsymbol{J}$	the Jacobian
$\boldsymbol{K}_{element}$	the element stiffness matrix
$\boldsymbol{R}_{element}$	the element residual vector
$\boldsymbol{t}_n$	the normal vector of the midplane of the cohesive element
$\boldsymbol{t}_1, \boldsymbol{t}_2$	the tangential vectors of the midplane of the cohesive element

$Node_{newid}$	the new node identifier
$node_{tot}$	the total number of nodes
$Grain_{id}$	the grain identifier
$Node_{oldid}$	the old node identifier
FEAP	Finite Element Analysis Program
E	the Young's modulus
ν	the Poisson's ratio
σ_0	the yield stress
E_p	the hardening modulus

LIST OF FIGURES

LIST OF TABLES

CONTENTS

1 INTRODUCTION

Many materials, considered homogeneous on a macroscale, reveal their heterogeneity on a smaller scale. Microstructure is a complex of heterogeneous features of the material, which includes grain size, shape and orientation, i.e. grain morphology; structural defects such as grain boundaries, dislocations, cracks, etc. Studying and understanding the material properties and behavior on a microscale is essential to predict its behavior on a macroscale. The aim of this thesis is to create the framework that gives the possibility to study how different grain morphologies in the microstructure affect the propagation of intergranular fracture in the coating layer.

Coating layer is a layer covering the base material, which is usually referred to as the substrate. Coatings can be decorative or functional. Decorative coatings are general paints and lacquers. Functional coatings can change surface properties of the substrate like wear and corrosion resistance, adhesion and wettability. They are several ways of applying the coating: vapor deposition, chemical and electrochemical techniques, spraying, roll-to-roll processes. In this thesis, a coating, which is applied on the substrate by High Power Pulsed Magnetron Sputtering (HPPMS), serves as a prototype for generating the model to analyze. HPPMS is an advanced and recent method for physical vapor deposition of thin films, which has many parameters leading to optimizing the coating layer structure. The usual thickness of the coating layer produced by HPPMS is several μm. Advantages and detailed description of this method can be found in (Sarakinos, Alami & Konstantinidis 2010).

Grain boundary is a region that separates two crystals of the same phase (Lejcek 2010). Intergranular fracture happens along grain boundaries. Cohesive Zone Modelling (CZM) is a widely used approach to simulate intergranular fracture initiation and evolution (Sfantos & Aliabadi 2007), (Paggi & Wriggers 2011), (Simonovski & Cizelj 2015). The concept of CZM was introduced in (Barenblatt 1962), which describes the fracture behavior of perfectly brittle materials. Cohesive elements describe interface traction between grains as a function of opening displacement according to Traction-Separation law (TSL). Several types of TSL were introduced in the past: exponential type (Needleman 1990), trapezoidal type (Tvergaard & Hutchinson 1992), linear type (Camacho & Ortiz 1996), bilinear type (Geubelle & Baylor 1998). Chapter 3 explains the theory behind cohesive elements and section 4.2.1 describes the method for adding cohesive elements into a finite element model.

There are two major methods of obtaining three-dimensional digital model of the microstructure. One way is using an actually existing material specimen and obtaining the microstructure model with for example X-ray computer tomography. Figure 1 illustrates the principle of this method. A detailed description of principles and applications of the method explained in (Salvo, Suéry, Marmottant, Limodin & Bernard 2010), (Beckmann, Grupp, Haibel, Huppmann, Nöthe, Pyzalla, Reimers, Schreyer & Zettler

2007). The main limitation one faces when using X-ray tomography is that in order to obtain a microstructure model with a different grain geometry and size one should find and use a material specimen with desired characteristics.

The other way is using mathematical tools to generate the microstructure model. Using mathematics gives the flexibility of generation a various number of different microstructure models with desired morphology in a short time. Such mathematical tool that is used in approximating a real microstructure is called Voronoi diagram or tessellation. The origin of the Voronoi diagram dates back to the 17th century when René Descartes claimed in his book that the solar system space consists of vortices (Descartes 1644). His illustrations show a space divided into convex regions, regions of influence for each star. The mathematician Georgy Voronoy was the first who formally described the subdivision of space into regions of influence in his work (Voronoy 1908). Chapter 2 of this thesis describes in details the theory and implementation of the Voronoi diagram in polycrystalline microstructure modelling.

To study the effect of different grain morphology on damage initialization and propagation in the coating layer, a nanoindentation and tensile tests are simulated using finite element method. The nanoindentation test is a form of hardness test used to measure hardness of thin films, micro- and nanostructures (Poon, Rittel & Ravichandran 2008). Chapter 5 describes the problem setup for the finite element analysis and chapter 6 represents the results of the analyses. Figure 2 represents the step-by-step process that was followed in this thesis.

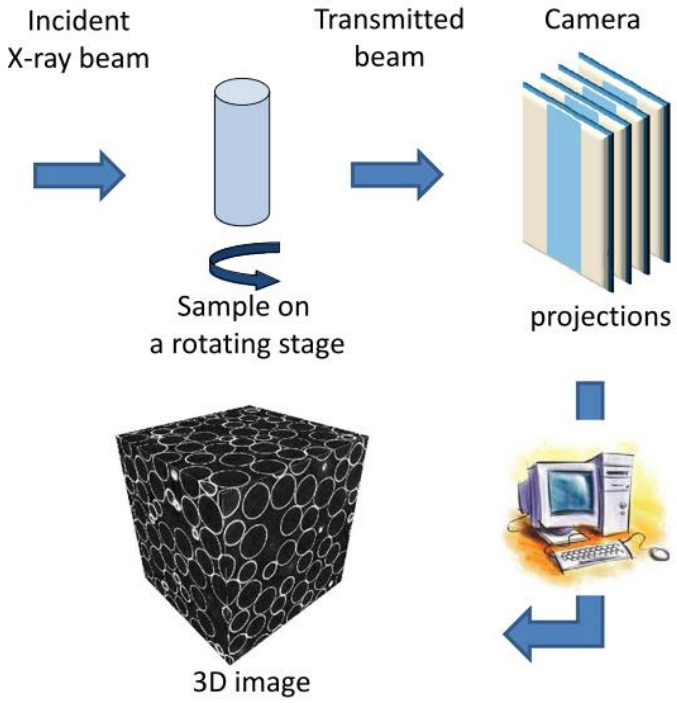

Figure 1 Principle of X-ray tomography (Salvo et al. 2010).

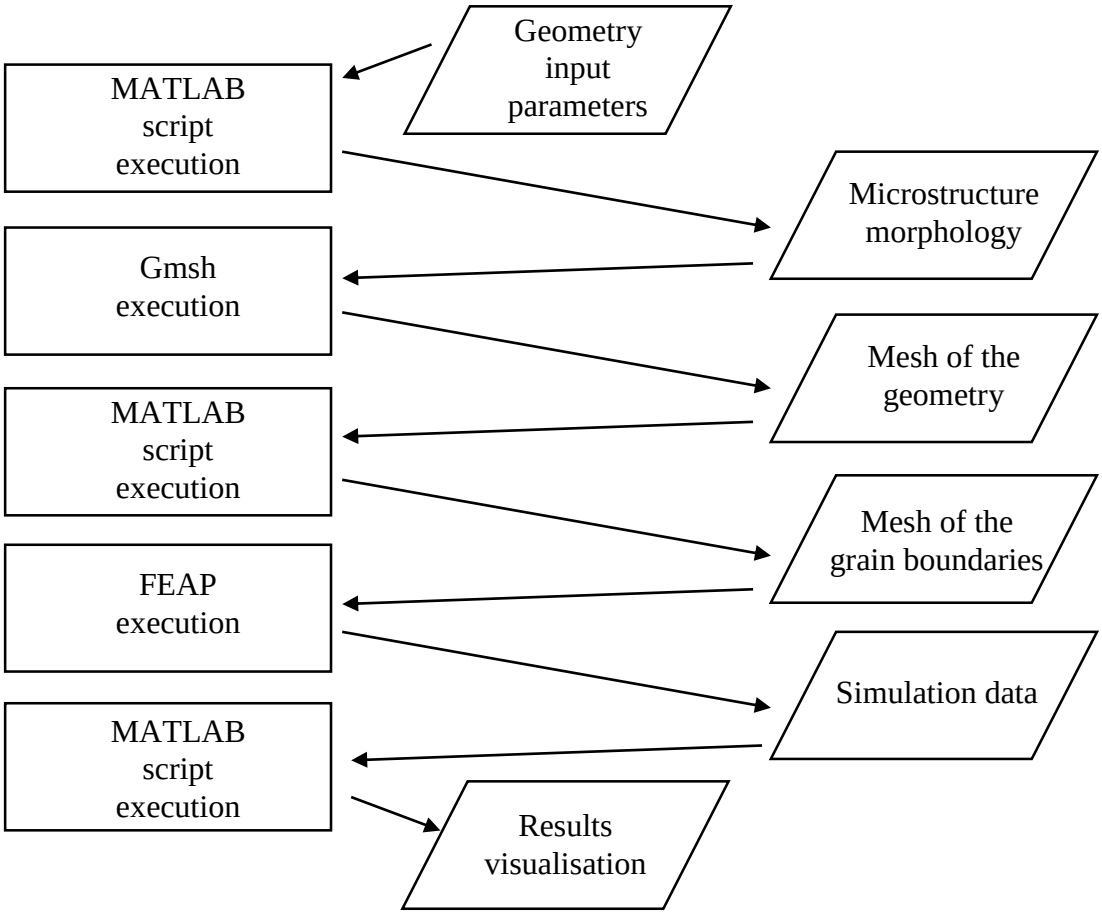

Figure 2 Flowchart of the working process

2 GEOMETRY GENERATION OF MICROSTRUCTURE

On a microstructure level, many materials are composed of crystallites of various size and orientation. Those crystallites are also referred to as grains. A common method of generating a microstructure polycrystalline model is approximating it with the Voronoi diagram.

2.1 Spatial tessellations

Spatial tessellation is the tiling of the space with geometric shapes without leaving any region uncovered (Schwartzman 1996). Two types of spatial tessellation were used in this thesis: Voronoi diagram and Delaunay triangulation.

2.1.1 Voronoi diagram

The Voronoi diagram is a tessellation of the space into n set of regions (R_i) associated with given seed points (P_i), so that any location within the region is closer to the associated seed point than to any other:

$$R_i = \{x \in \mathbb{R}^d : \|P_i - x\| < \|P_j - x\| \ \ \forall i \neq j \ \ i, j = 1, \dots, n\}$$

The name of those regions is Voronoi cells. Voronoi cells have the shape of convex polygon in two dimensions and convex polyhedron in three dimensions. They are referred to as the grains of a microstructure. One of the important properties of the Voronoi diagram is its duality with Delaunay triangulation. That means that knowing for example Delaunay triangulation for a given set of points Voronoi diagram can be found and vice versa. (Okabe, Boots, Sugihara & Chiu 2000)

2.1.2 Delaunay triangulation

A triangulation of a set of points (P) is a planar subdivision whose bounded faces are triangles and whose vertices are the points in P. Particularly, Delaunay triangulation of a set P of points in a three-dimensional space is a triangulation $DT(P)$ such that no point in P is inside the circumsphere of any tetrahedron in $DT(P)$.

Delaunay triangulation has a variety of applications in various fields where subdivision into triangles is required due to its property of maximizing the minimum angle, i.e. it tends to avoid skinny triangles (Berg, Cheong, Kreveld & Overmars 2008).

2.2 MATLAB implementation

A MATLAB (MathWorks 2016) script was developed to generate the three-dimensional microstructure polycrystalline model with six input

parameters, which control the size of the model and number of grains in the model.

```
%%input parameters
Lx=ℤ⁺; %length of the boundary domain in x-direction
Ly=ℤ⁺; %length of the boundary domain in y-direction
Lz=ℤ⁺; %length of the boundary domain in z-direction
Nx=ℤ⁺; %number of grains in x-direction
Ny=ℤ⁺; %number of grains in y-direction
Nz=ℤ⁺; %number of grains in z-direction
```

The following steps were implemented in MATLAB:

- Creating a set of seed points,
- Performing Delaunay triangulation of the given set of seed points,
- Obtaining Voronoi diagram from the Delaunay triangulation,
- Exporting the Voronoi diagram data for post-processing.

2.2.1 Creating a set of seed points

Size and shape of Voronoi cells depend on a number of seed points and a distance between them. Therefore, control over positioning of the seed points should be implemented to get control over the cell morphology. The following algorithm was used for that purpose:

- In x, y, z-directions the domain is divided into Nx, Ny, Nz number of grid regions respectively, where $Nx \cdot Ny \cdot Nz$ equals to the total number of seed points;

```
%%dividing the domain into grid regions
stepx=Lx/Nx;
stepy=Ly/Ny;
stepz=Lz/Nz;
```

- Rectangular grid hexahedrons are formed;
- Seed points are randomly generated within the first hexahedron (Figure 3a);

```
%%generating random seed points
for i=1:(Nx*Ny*Nz)
     pos_init(i,:)=[stepx.*rand(1,1) stepy.*rand(1,1)
     stepz.*rand(1,1)];
end
```

- Seed points are distributed in the domain so that every grid hexahedron contains only one seed point (Figure 3b).

```
%%distributing the seed points within the domain
pos_stepx=[repmat((0:(Nx-
1))'.*stepx,((Nx*Ny*Nz)/size((0:(Nx-1))',1)),1)
zeros((Nx*Ny*Nz),1) zeros((Nx*Ny*Nz),1)];
pos_stepy=[zeros(Nx*Ny*Nz,1) repelem([(0:(Ny-
1))'.*stepy],((Nx*Ny*Nz)/size((0:(Ny-1))',1)))
zeros(Nx*Ny*Nz,1)];
pos_stepz=[zeros(Nx*Ny*Nz,1) zeros(Nx*Ny*Nz,1)
repmat([(0:(Nz-1))'.*stepz],((Nx*Ny*Nz)/size((0:(Nz-
1))',1)),1)];
pos=pos_stepx+pos_stepy+pos_stepz;
```

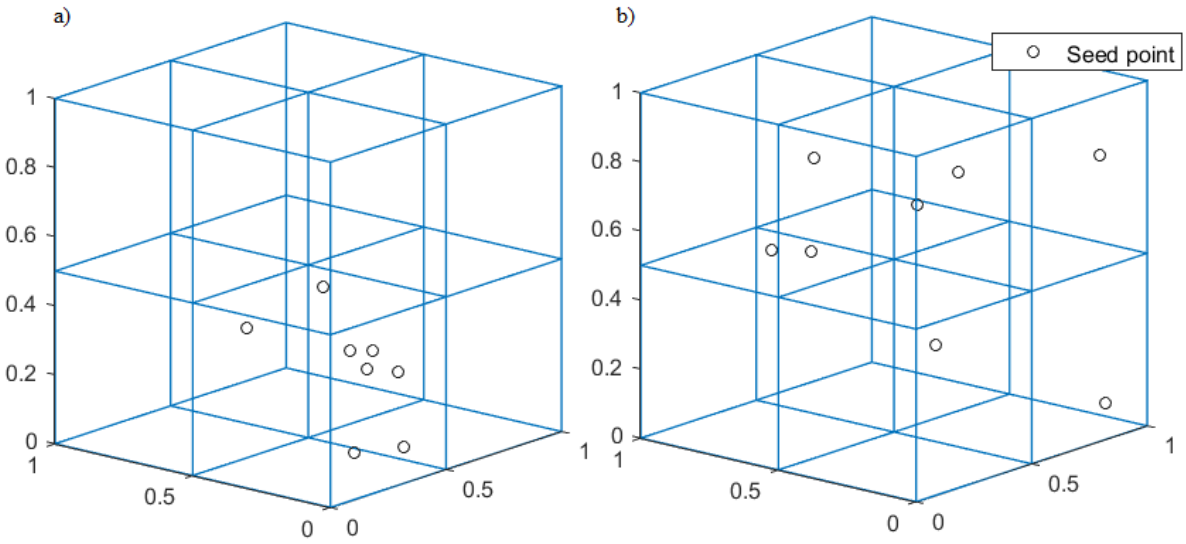

Figure 3 Positioning of eight seed points a) within the first hexahedron b) within the whole domain. Grid size chosen to be equal in all directions.

2.2.2 Performing Delaunay triangulation of the given set of seed points

Triangulation is performed with the MATLAB `delaunayTriangulation` class. Using this class gives the opportunity to perform a variety of topological and geometric queries. MATLAB computes Delaunay triangulation based on Qhull algorithm. (MathWorks 2016)

```
%%triangulation of the seed points
DT=delaunayTriangulation(pos(:,1),pos(:,2),pos(:,3));
```

2.2.3 Obtaining Voronoi diagram from the Delaunay triangulation

Straight line dual connection of the Delaunay triangulation and Voronoi diagram gives the fact that intersection of perpendicular bisectors of the given triangle forms a Voronoi vertex (Okabe et al. 2000).

For every given seed point all attached triangles are found with `vertexAttachments`. A set of intersections of perpendicular bisectors of attached triangles gives a set of Voronoi vertices for a given seed point (Figure 4).

```
%%finding neighboring vertices for each vertex
for i=1:size(pos,1); k=0;
    VA(i)=vertexAttachments(DT,i);
    for j=1:size(VA{i},2);
        k=k+1;
        VA1{i}(k,:)=setdiff(DT(VA{1,i}(j),:),i);
    end
    neib{i}=unique(VA1{i});
end
```

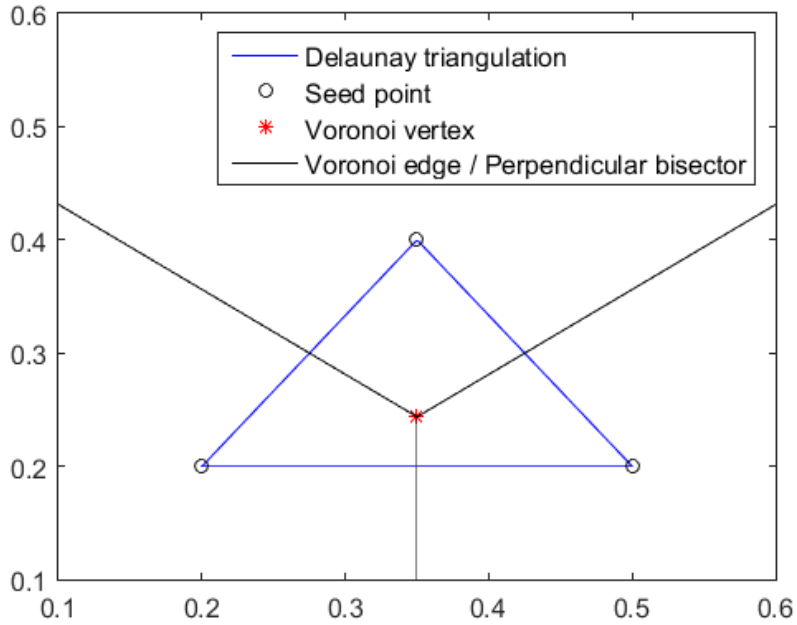

Figure 4 Obtaining Voronoi vertex from Delaunay triangulation

```
%%finding vertices of the voronoi regions
for i=1:size(pos,1)
    for j=1:size(vor{i},2)
        vorvertex{i}=mean(pos(i,:), pos(vor{i}(j),:));
    end
end
```

Knowing vertices of the Voronoi cell, a convex hull is obtained with `convhulln` function. A set of convex hulls forms a Voronoi diagram (Figure 5).

```
for i=1:size(pos,1)
    K{i}=convhulln(vorvertex{i});
end
```

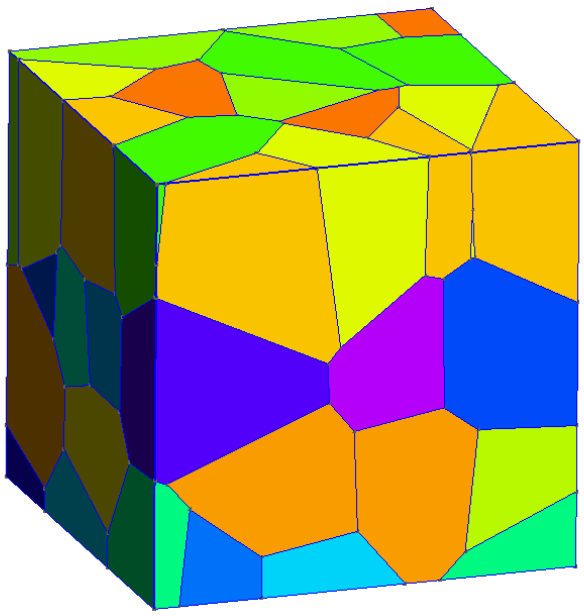

Figure 5 Voronoi diagram of 64 seed points

2.3 Coating-substrate system

HPPMS coating process provides dense columnar grain structure, where grains grow from the substrate (Figure 6).

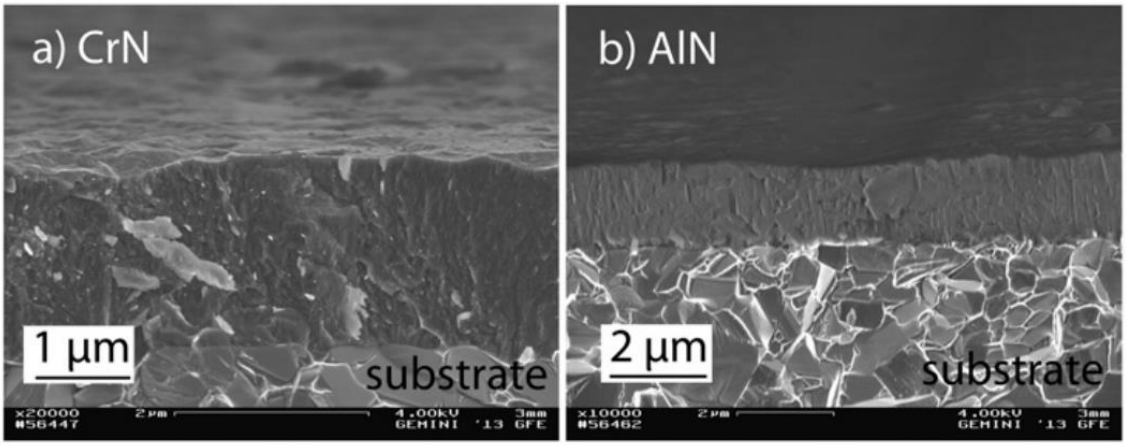

Figure 6 SEM cross section fracture images of CrN (a), AlN (b) (Bobzin, Brögelmann, Brugnara, Arghavani, Yang, Chang & Chang 2015)

An approximated digital three-dimensional model of HPPMS processed coating is obtained with the MATLAB script by controlling the input parameters. In this work, microstructure morphology is assigned only to the coating layer and the substrate is modelled as a solid brick.

Figure 7 illustrates the coating-substrate model that is generated with the developed script. Input parameters for the coating microstructure are $Lx = 10,\ Ly = 10,\ Lz = 3,\ Nx = 20,\ Ny = 20,\ Nz = 3$.

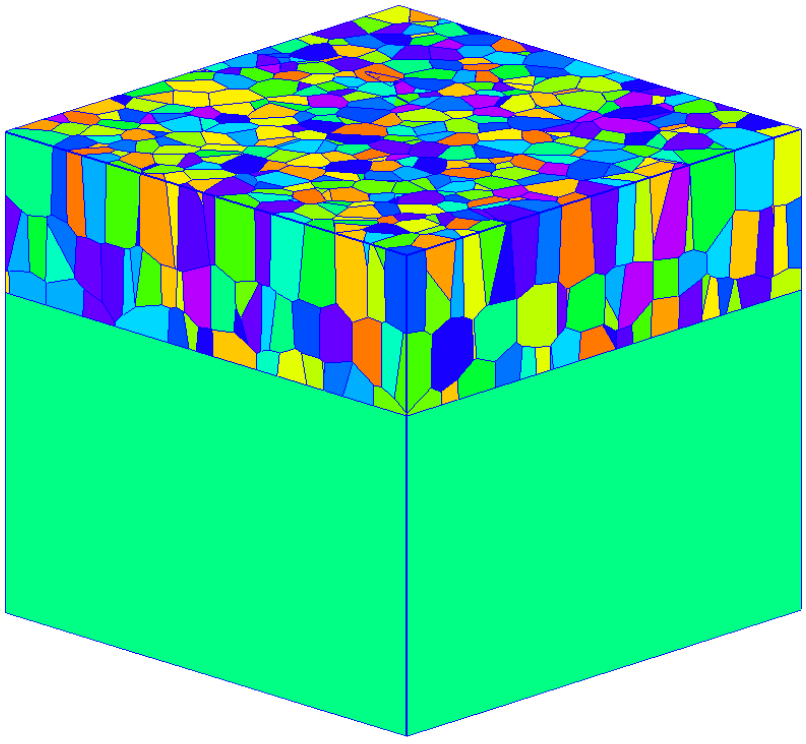

Figure 7 An example of the generated coating-substrate system model

3 MECHANICS OF COHESIVE ZONE ELEMENTS

Cohesive zone elements are the elements that do not describe any physical material but instead they represent forces, which occur between two material surfaces being pulled out. Behavior of the material separation is based on Traction-Separation law (TSL). In this thesis, bi-linear TSL is used (Figure 8).

The traction stress vector $\boldsymbol{t}$ consists of three components: t_n, t_{s1}, t_{s2} which represent the normal and the two shear tractions respectively. The corresponding separations are denoted by $\delta_n, \delta_{s1}, \delta_{s2}$.

3.1 Traction-Separation law

Description of the damage and failure mechanism in cohesive elements consists of three parts:

- the undamaged behavior,
- the damage initiation,
- the damage evolution.

3.1.1 Undamaged behavior

Prior to damage, the cohesive element follows linear behavior and traction vector is described as:

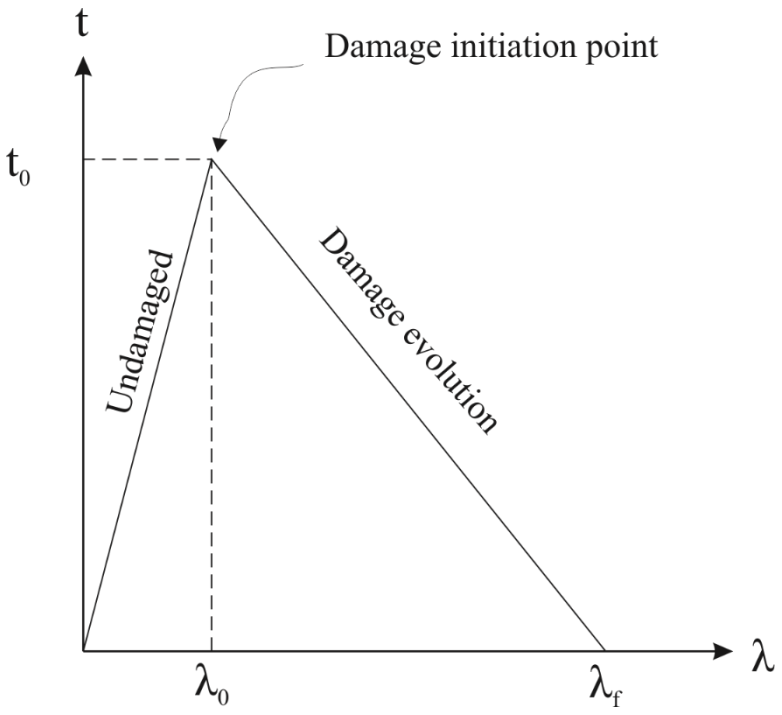

Figure 8 Bi-linear Traction-Separation law

$$\boldsymbol{t} = \begin{Bmatrix} t_n \\ t_{s1} \\ t_{s2} \end{Bmatrix} = \begin{bmatrix} \frac{\partial t_n}{\partial \delta_n} & \frac{\partial t_n}{\partial \delta_{s1}} & \frac{\partial t_n}{\partial \delta_{s2}} \\ \frac{\partial t_n}{\partial \delta_{s1}} & \frac{\partial t_{s1}}{\partial \delta_{s1}} & \frac{\partial t_{s1}}{\partial \delta_{s2}} \\ \frac{\partial t_n}{\partial \delta_{s2}} & \frac{\partial t_{s1}}{\partial \delta_{s2}} & \frac{\partial t_{s2}}{\partial \delta_{s2}} \end{bmatrix} \begin{Bmatrix} \delta_n \\ \delta_{s1} \\ \delta_{s2} \end{Bmatrix} = \boldsymbol{K\delta}$$

3.1.2 Damage initiation

The damage initiation criterion is the point that refers to the beginning of degradation in interface element. Damage initializes when the effective separation (λ) becomes equal to the effective separation at initiation of damage (λ_0). The effective separation is defined as:

$$\lambda = \sqrt{\langle \delta_n \rangle^2 + \beta^2 (\delta_{s1}^2 + \delta_{s2}^2)}$$

The parameter β denotes the ratio of shear to normal strengths. An assumption here is that, the behaviors of separation in normal and shear directions are identical, i.e., interfacial strength is identical in all in-plane directions.

The Macaulay brackets $\langle\ \rangle$ show that there is no damage in case of pure normal compression.

3.1.3 Damage evolution

The damage evolution law represents the rate at which material stiffness is degraded once damage initiation criterion is met. The amount of damage in the interface is described by a scalar damage variable (D), which varies from 0 to 1. The evolution of D is expressed as a function of effective separation (λ) between effective separation at initiation of damage (λ_0) and effective separation at complete failure (λ_f) (Figure 9).

For the bi-linear TSL, the damage variable is defined as:

$$D = \begin{cases} 0, & \lambda < \lambda_0 \\ \dfrac{\lambda_f}{\lambda_f - \lambda_0} \dfrac{\lambda - \lambda_0}{\lambda}, & \lambda_0 < \lambda < \lambda_f \\ 1, & \lambda_f < \lambda \end{cases}$$

Then the expression for traction vector is given by:

$$\boldsymbol{t}_D = (1 - D)\boldsymbol{t}$$

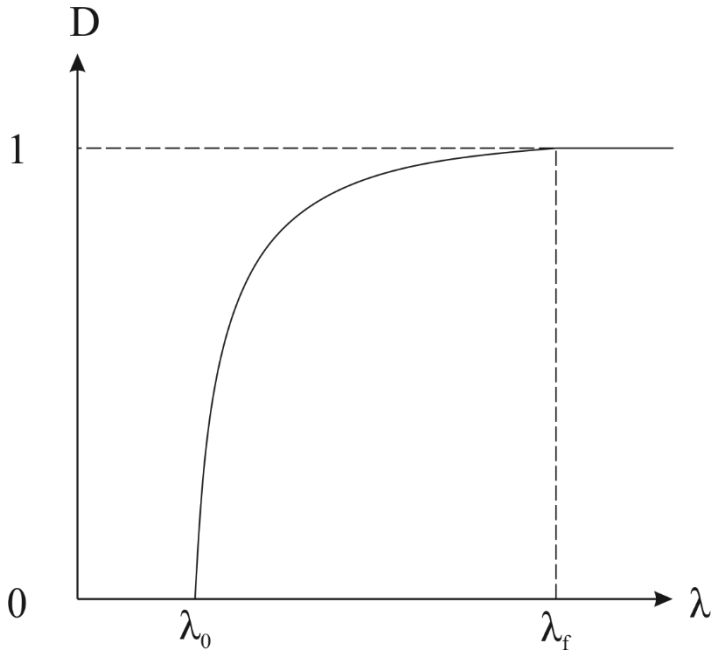

Figure 9 Damage evolution

3.2 Finite element formulation

Finite element formulation of cohesive element is described by using the principle of virtual work (Hughes 1987):

$$W_{int} = \int_{\Omega} \delta \boldsymbol{E} : \boldsymbol{S} dV = \int_{\Gamma} \delta \boldsymbol{u} \cdot \boldsymbol{T}_{ext} d\Gamma = W_{ext}$$

where $\boldsymbol{E}$ is the Green strain tensor in the domain Ω; $\delta \boldsymbol{u}$ is the virtual displacement on the boundary Γ; $\boldsymbol{T}_{ext}$ is the external traction; $\boldsymbol{S}$ is the second Piola-Kirchhoff stress tensor.

Cohesive element contributes an additional term to the internal work:

$$\int_{\Omega} \delta \boldsymbol{E} : \boldsymbol{S} dV + \int_{\Gamma_c} \delta \boldsymbol{\Delta} \cdot \boldsymbol{T}_c d\Gamma_c = \int_{\Gamma} \delta \boldsymbol{u} \cdot \boldsymbol{T}_{ext} d\Gamma$$

where $\boldsymbol{T}_c$ is the cohesive traction along the fracture surface Γ_c; $\delta \boldsymbol{\Delta}$ is the virtual separation.

The contribution from cohesive element is discretized with the Galerkin method (Brenner & Scott 2008):

$$\boldsymbol{K}_{element} = \int_{-1}^{1} \int_{-1}^{1} \boldsymbol{B}^T \boldsymbol{\Theta}^T \boldsymbol{K}_{local} \boldsymbol{\Theta} \boldsymbol{B} \det \boldsymbol{J} \; d\xi d\eta$$

$$\boldsymbol{R}_{element} = \int_{-1}^{1} \int_{-1}^{1} \boldsymbol{B}^T \boldsymbol{\Theta}^T \boldsymbol{t}_{local} \det \boldsymbol{J} \; d\xi d\eta$$

where ξ, η denote local coordinates; $\boldsymbol{B}$ is the global displacement-separation matrix that computes relative gap of the crack at any point in the cohesive element; $\boldsymbol{\Theta}$ is the transformation tensor; $\boldsymbol{K}_{local}$ and $\boldsymbol{t}_{local}$ are the local stiffness matrix and the local traction vector respectively; $\det \boldsymbol{J}$ is the Jacobian; $\boldsymbol{K}_{element}$ is the element stiffness matrix; $\boldsymbol{R}_{element}$ is the element residual vector.

The displacement-separation matrix $\boldsymbol{B}$ is computed from identity matrix $\boldsymbol{I}$ and shape functions $N_i(\xi, \eta)\ i = 1,2, \dots n$:

$$\boldsymbol{B} = [N_1(\xi,\eta)I_{3\text{x}3} \mid N_2(\xi,\eta)I_{3\text{x}3} \mid N_i(\xi,\eta)I_{3\text{x}3}][-I_{3nx3n} \mid I_{3nx3n}]$$

The transformation tensor $\boldsymbol{\Theta}$ is defined by direction cosines of the local coordinate system:

$$\boldsymbol{\Theta} = [\boldsymbol{t_1}\ \boldsymbol{t_2}\ \boldsymbol{t_n}]$$

where $\boldsymbol{t_1}, \boldsymbol{t_2}, \boldsymbol{t_n}$ are two perpendicular tangential vectors and the normal vector respectively of the midplane of the cohesive element (Figure 10).

$\boldsymbol{K}_{local}$ and $\boldsymbol{t}_{local}$ are computed from the Traction-Separation law:

$$\boldsymbol{K}_{local} = \begin{bmatrix} \frac{\partial t_n}{\partial \delta_n} & \frac{\partial t_n}{\partial \delta_{s1}} & \frac{\partial t_n}{\partial \delta_{s2}} \\ \frac{\partial t_n}{\partial \delta_{s1}} & \frac{\partial t_{s1}}{\partial \delta_{s1}} & \frac{\partial t_{s1}}{\partial \delta_{s2}} \\ \frac{\partial t_n}{\partial \delta_{s2}} & \frac{\partial t_{s1}}{\partial \delta_{s2}} & \frac{\partial t_{s2}}{\partial \delta_{s2}} \end{bmatrix}$$

$$\boldsymbol{t}_{local} = \begin{Bmatrix} t_n \\ t_{s1} \\ t_{s2} \end{Bmatrix}$$

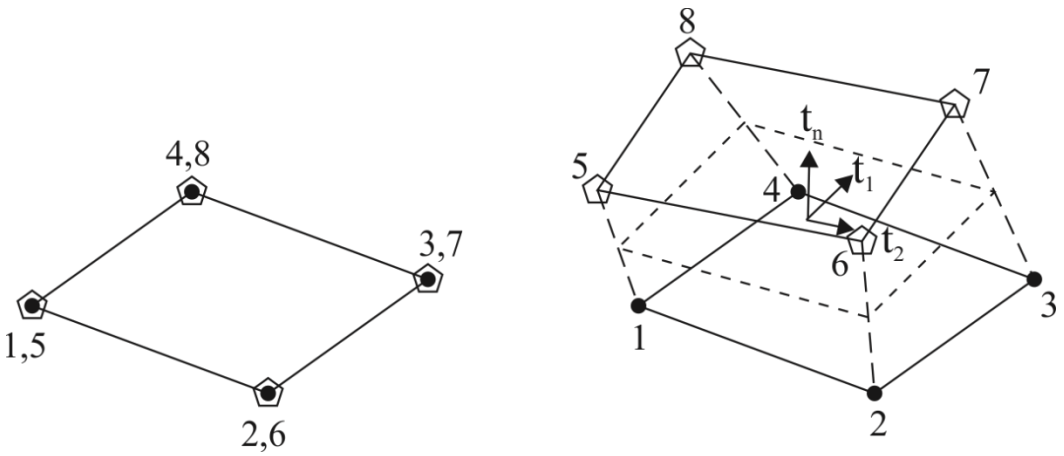

Figure 10 A cohesive element in the initial and deformed state

4 FINITE ELEMENT MODEL

This chapter describes steps of preparing the model for finite element analysis from mesh generation to applying boundary conditions.

4.1 Discretizing the domain

The first step of any numerical analysis method is discretization of the domain. In finite element method, the equivalent term for discretization of the domain is mesh generation or meshing. For this purpose open-source software Gmsh was used.

A finite element mesh is a tessellation of a given subset of the three-dimensional space by elementary geometrical elements of various shapes (in Gmsh's case: lines, triangles, quadrangles, tetrahedra, prisms, hexahedra and pyramids), arranged in such a way that if two of them intersect, they do so along a face, an edge or a node, and never otherwise. (Geuzaine & Remacle 2016). Gmsh uses bottom-up meshing strategy. Meshing starts in lowest dimension and then these elements are used to generate elements of higher dimension (Figure 11).

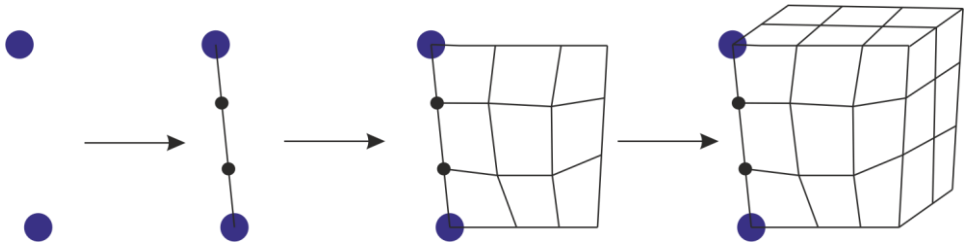

Figure 11 Bottom-up meshing strategy

Gmsh output file contains all the nodes and connectivity of the nodes into elements. In addition, it defines different element sets for different grain and different node sets for different grain faces. This is used later to modify the mesh.

4.2 Grain boundary mechanisms

In polycrystalline materials, different interaction mechanisms between the grains can have significant effects on the macroscopic behavior of the material (Kheradmand, Barnoush & Vehof 2010). These effects should be taken into account while generating the finite element model. Therefore, elements that are called cohesive should be added between the grains.

4.2.1 Adding cohesive zone elements

A MATLAB script was written that parses the Gmsh generated mesh file of the microstructure model and adds cohesive elements into the mesh. Grains need to be separated from each other, so that they do not share any node. Then grains are connected with zero thickness cohesive elements. Insertion

of cohesive elements between the grains was implemented with the following algorithm:

- Create a set of shared faces. All grain faces that do not lay on a boundary are considered to be shared faces.

```
%%creating a set of shared faces
%vector nodesFace{n} contains node identifiers of n-th
face
for i=1:size(nodesFace,2)
    sfid=nodesFace{i};
    nr=range(nodes(sfid,2:4));
    if nr(1)~=0 && nr(2)~=0 && nr(3)~=0
       sharedfaces(i,:)=i;
    end
end
sharedfaces=unique(sharedfaces);
```

- For every shared face, determine to which two grains it belongs.

```
%%assigning grains to the shared faces
%vector 'nodesGrain{n}' contains node identifiers of n-
th grain; matrix 'face' contains the data of 2D mesh
from Gmsh generated mesh file
k=0;
for i=1:size(nodesGrain,2)
    for j=1:size(sharedfaces,1)
        id=find(face(:,5)==sharedfaces(j));
        md=unique(mode(face(id,6:8)));
        inmd=intersect(md,nodesGrain{i});
        if length(md)==length(inmd)
            k=k+1;
            grainSharedfaces{j}(k,:)=i;
        end
    end
end
for i=1:size(grainSharedfaces,2)
    grainSharedfaces{i}=unique(grainSharedfaces{i});
end
```

- For every set of nodes of a given shared face, create two new sets of nodes by copying. Assign new node identifiers for them.

```
%%creating new nodes
k=0;
for i=sharedfaces'
    k=k+1;
    for j=1:size(nodesFace{i},1)
        nodesfacecopy{k,:}=nodes(nodesFace{i},:);
    end
    nodesfacecopyG1{k}=nodesfacecopy{k};
    nodesfacecopyG2{k}=nodesfacecopy{k};
    for j=1:size(nodesfacecopy{k},1)
        nodesfacecopyG1{k}(j,1)=grainSharedfaces{k}(1)*
        nnodes+nodesfacecopy{k}(j,1);
    end
    for j=1:size(nodesfacecopy{k},1)
        nodesfacecopyG2{k}(j,1)=grainSharedfaces{k}(2)*
        nnodes+nodesfacecopy{k}(j,1);
    end
end
```

- For every set of elements of a given shared face, create two new sets of elements by copying. Assign new node identifiers for them.

```
%%creating new face elements
for i=sharedfaces'
    idface=find(face(:,5)==i;
    facecopy{k}=face(idface,:);
    for j=1:size(face1{k},1)
        faceG1{k}(j,:)=grainSharedfaces{k}(1)*nnodes+
        facecopy{k}(j,:);
    end
    for j=1:size(face1{k},1)
        faceG2{k}(j,:)=grainSharedfaces{k}(2)*nnodes+
        facecopy{k}(j,:);
    end
end
```

- For every volume element find nodes that are the part of a given shared face. Assign new node identifiers for them.

```
%%creating new volume elements
%matrix 'volume' contains the data of 3D mesh from Gmsh
generated mesh file
%fifth column of this matrix contains the data to which
grain the element is assigned
newvolume=volume;
idv=unique(cell2mat(facecopy'));
for i=1:size(idv,1)
    if ~isempty(find(newvolume==idv(i)))
       [row col]=find(newvolume==idv(i));
       for h=1:size(row,1)
           newvolume(row(h),col(h))=newvolume(row(h),5)*
           nnodes+idv(i);
       end
    end
end
```

- For every two new set of elements, by merging into one set create a set of cohesive elements.

```
%%creating a set of cohesive element
cohesivelist=cell2mat([faceG1;faceG2]');
```

Assigning new node identifiers is handled with the following function:

$$Node_{newid} = Grain_{id} \cdot node_{tot} + Node_{oldid}$$

where $Node_{newid}$ is the new node identifier; $node_{tot}$ is the total number of nodes in the Gmsh generated mesh; $Grain_{id}$ is the grain identifier; $Node_{oldid}$ is the old node identifier.

Figure 12 represents the result of above described algorithm.

The developed script is suitable for inserting cohesive elements into both quadrilateral and triangular mesh.

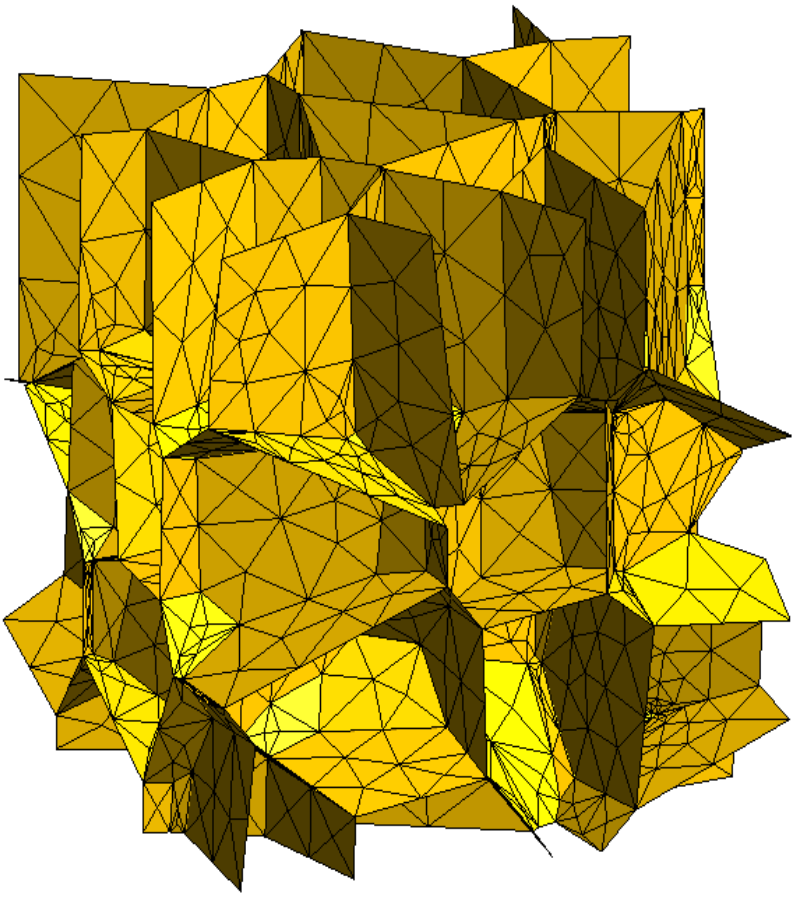

Figure 12 Cohesive elements of 64-grain geometry with hidden grains

5 PROBLEM SETUP

In order to verify the generated model and study the material behavior under loads two different test cases were prepared for simulations with Finite Element Analysis Program (FEAP) developed in UC Berkeley (Taylor 2015). Size of the generated microstructure model was set to:

- $Lx = 10,\ Ly = 3,\ Lz = 2$ for the tensile test,
- $Lx = 2,\ Ly = 2,\ Lz = 2$ for the nanoindentation test.

5.1 Tensile test

A coating-substrate system was simulated to experience uniaxial tensile load in a larger structure. Displacement boundary conditions of certain nodes of the system were prescribed so that nodes on the left face were restricted to move in x-direction and the displacement to the x^+ direction was applied on the right face of the model (Figure 13).

Apart boundary conditions another essential part of finite element model is assigning material properties for every element within a model. The material for the substrate elements was chosen to be steel with Young's modulus $E = 210$ GPa, Poisson's ratio $\nu = 0.3$, and yield stress $\sigma_0 = 200$ MPa. The substrate material is the same though all the simulations. For the coating elements, two different sets of material parameters were used in the simulations, in order to verify that damage propagation is dependent on a material. One material was chosen to be ductile and the other one to be brittle. The properties for the first set were set to: Young's modulus $E = 450$ GPa, Poisson's ratio $\nu = 0.2$, yield stress $\sigma_0 = 2$ GPa, hardening modulus $E_p = 18$ GPa. For the second set — Young's modulus $E = 350$ GPa, Poisson's ratio $\nu = 0.25$, yield stress $\sigma_0 = 4$ GPa, hardening modulus $E_p = 14$ GPa. Material properties for the cohesive elements between grains in the coating are set to: cohesive strength $t_0 = 2$ GPa for

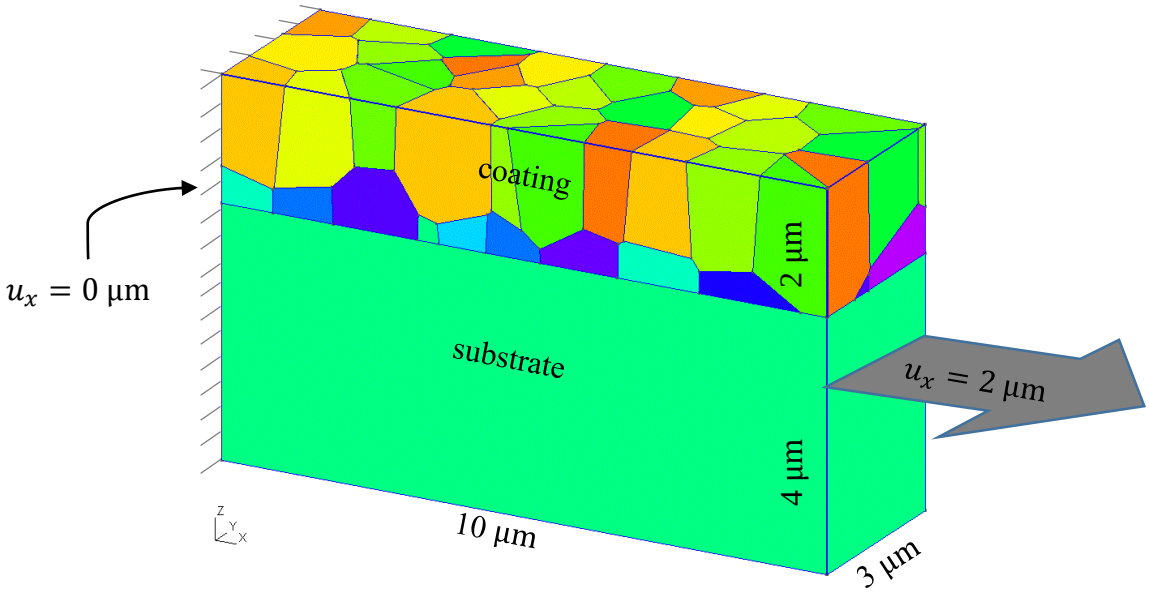

Figure 13 Tensile test load case

the first coating material set and $t_0 = 1.5$ GPa for the second coating material set, for both sets effective separation at damage initiation $\lambda_0 = 0.01$ μm, effective separation at complete failure $\lambda_f = 0.1$ μm, ratio shear to normal traction $\beta = 1$. In order to reduce the effect of delamination in the system cohesive strength of cohesive zone elements between the substrate and the coating was set to ten times higher than inside the coating in all simulations. Material properties are summarized in Table 1.

Table 1 Material properties for the tensile test

Solid element properties				
	E [GPa]	ν [-]	σ_0 [GPa]	E_p [GPa]
Substrate	210	0.3	200	-
Coating #1	450	0.2	2	18
Coating #2	350	0.25	4	14
Cohesive element properties				
	t_0 [GPa]	λ_0 [μm]	λ_f [μm]	β [-]
Coating #1	2	0.01	0.1	1
Coating #2	1.5	0.01	0.1	1

Two comparison sets of simulations were performed of the tensile test:

- the coating morphology is kept constant and the effect of changing the coating material parameters is studied.
- the material parameters are kept constant and the effect of changing the microstructure morphology is studied.

For the first set of simulations, input parameters for the coating microstructure generation were set to $Nx = 10,\ Ny = 3,\ Nz = 2$. For the second set number of grains in y direction $Ny = 3$ and z direction $Nz = 1$ were kept constant while number of grains along tensile load in x direction was set to $Nx = \{5,10,15,25\}$. Table 2 gathers the information about different simulations runs.

Table 2 Description of the tensile test simulations

Simulation set	Simulation ID	Material properties	Grain morphology		
			Nx	Ny	Nz
I	1	Coating #1	10	3	2
	2	Coating #2	10	3	2
II	3	Coating #1	5	3	1
	4	Coating #1	10	3	1
	5	Coating #1	15	3	1
	6	Coating #1	25	3	1

5.2 Nanoindentation test

A nanoindentation test of the coating-substrate system model was simulated. For ease of the contact computation one fourth of the model was simulated (Figure 14). Boundary conditions were set so that at $x = 0$ displacement $u_x = 0$, at $y = 0$ displacement $u_y = 0$, at bottom face of the substrate displacement $u_z = 0$ (Figure 15a). Stresses in the coating-substrate system are induced by contact interaction with spherical indentator, which is displaced in the z- direction ($u_z = -1$). Contact was defined by top face of the coating-substrate system and round face of the indentator (Figure 15b).

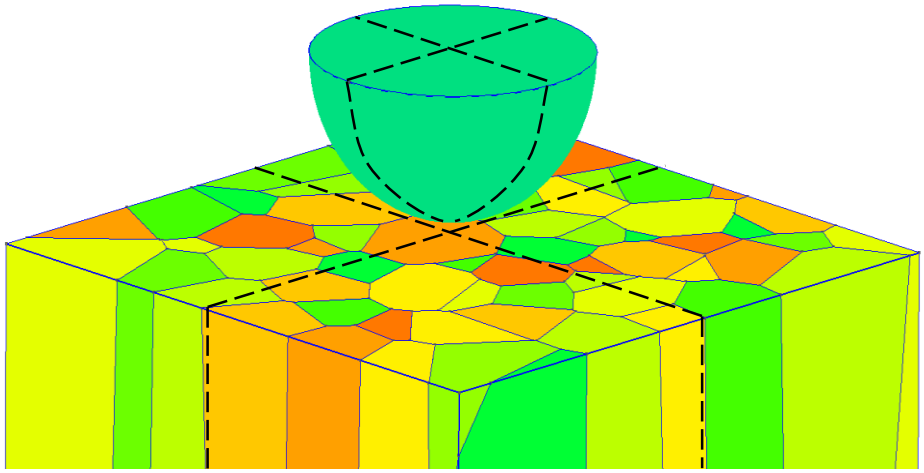

Figure 14 Dividing a model for the nanoindentation test

Material properties for the coating grain elements were set to: Young's modulus $E = 450$ GPa, Poisson's ratio $\nu = 0.2$, yield stress $\sigma_0 = 2$ GPa, hardening modulus $E_p = 18$ GPa. For the substrate — Young's modulus $E = 210$ GPa, Poisson's ratio $\nu = 0.3$, yield stress $\sigma_0 =$

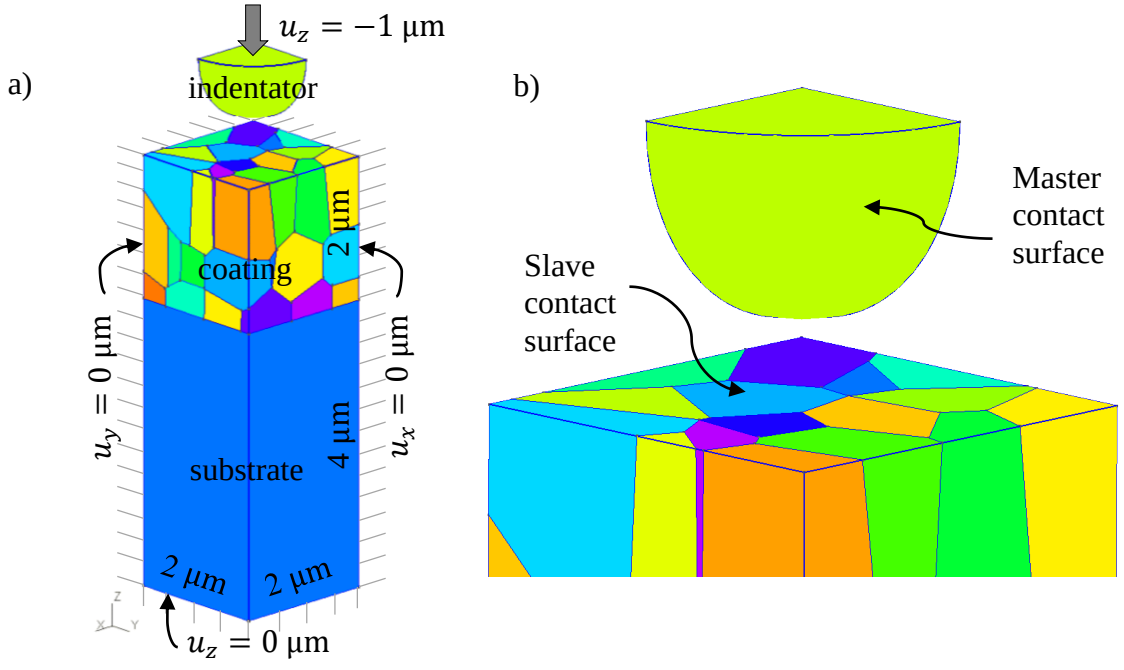

Figure 15 a) Nanoindentation test boundary conditions b) nanoindentation test contact surfaces

200 MPa. Material properties for the cohesive elements between grains in the coating are set to: cohesive strength $t_0 = 0.1$ GPa, effective separation at damage initiation $\lambda_0 = 0.01$ μm, effective separation at complete failure $\lambda_f = 0.1$ μm, ratio shear to normal traction $\beta = 1$. Material properties are summarized in Table 3.

Table 3 Material properties for the nanoindentation test

Solid element properties				
	E [GPa]	ν [-]	σ_0 [GPa]	E_p [GPa]
Substrate	210	0.3	200	-
Coating	450	0.2	2	18
Cohesive element properties				
	t_0 [GPa]	λ_0 [μm]	λ_f [μm]	β [-]
Coating	0.25	0.01	0.1	1

In nanoindentation test simulations, material parameters were kept constant through all the simulation runs and the effect of changing microstructure morphology is studied. Table 4 gathers the information about nanoindentation test simulations runs.

Table 4 Description of the nanoindentation test simulations

Simulation ID	Grain morphology		
	Nx	Ny	Nz
7	8	8	1
8	6	6	1
9	4	4	1
10	4	4	2

6 RESULTS

In order to verify that the generated coating-substrate geometry is working correctly and to study the crack propagation in the microstructure, a several simulation runs were performed with FEAP. The output of the FEAP simulations is data text files containing information about reaction forces, nodal coordinates of cohesive zone elements and element damage at each load step. A MATLAB script was made to process and visualize this data. Figure 16 describes the color map used to visualize the cohesive zone damage.

Figure 16 Color map for cohesive zone damage visualization

Reaction force graphs represent the reaction forces that occur at nodes of the face where load is applied at each load step. Maximum damage evolution graphs show the data of the biggest cohesive zone element damage value in the system at each load step. Mean damage evolution graphs show the average value cohesive zone element damage in the system at each load step.

6.1 Tensile test results

Simulation set I studies what effect changing material properties has on the results of the simulation. Figure 17 represents the resultant intergranular crack. From the obtained results, it is seen that for the same geometry the location of the crack initialization and propagation path remains the same. What is changing is the amount of damage caused in the system. From Figure 19 it is seen that the Simulation ID 2 has more brittle behavior compared to the Simulation ID 1. Simulation ID 2 reaches the first interface failure faster than the Simulation ID 1 (Figure 18) and overall mean damage in the system through the simulation run is higher in the Simulation ID 2 (Figure 21)

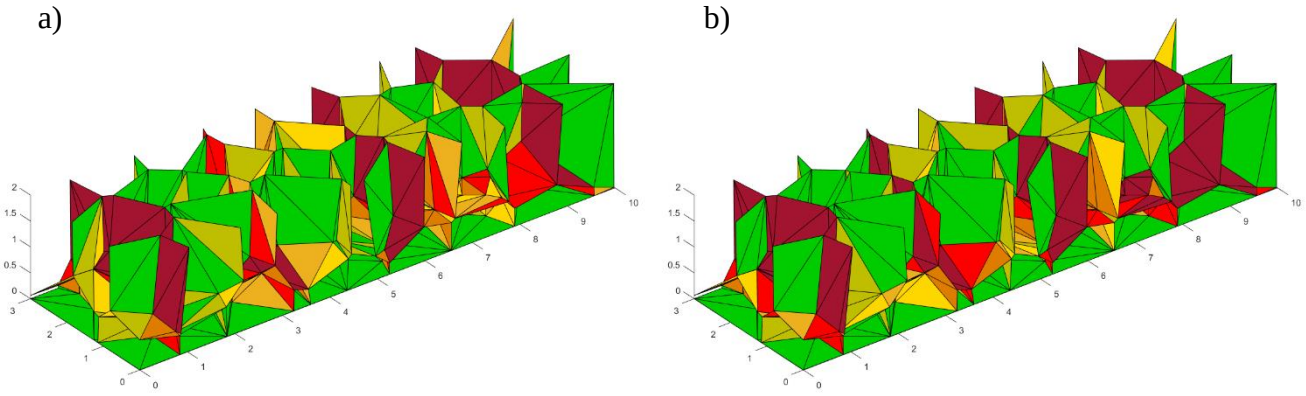

Figure 17 Isometric view of cohesive zone damage. a) Simulation ID 1 b) Simulation ID 2

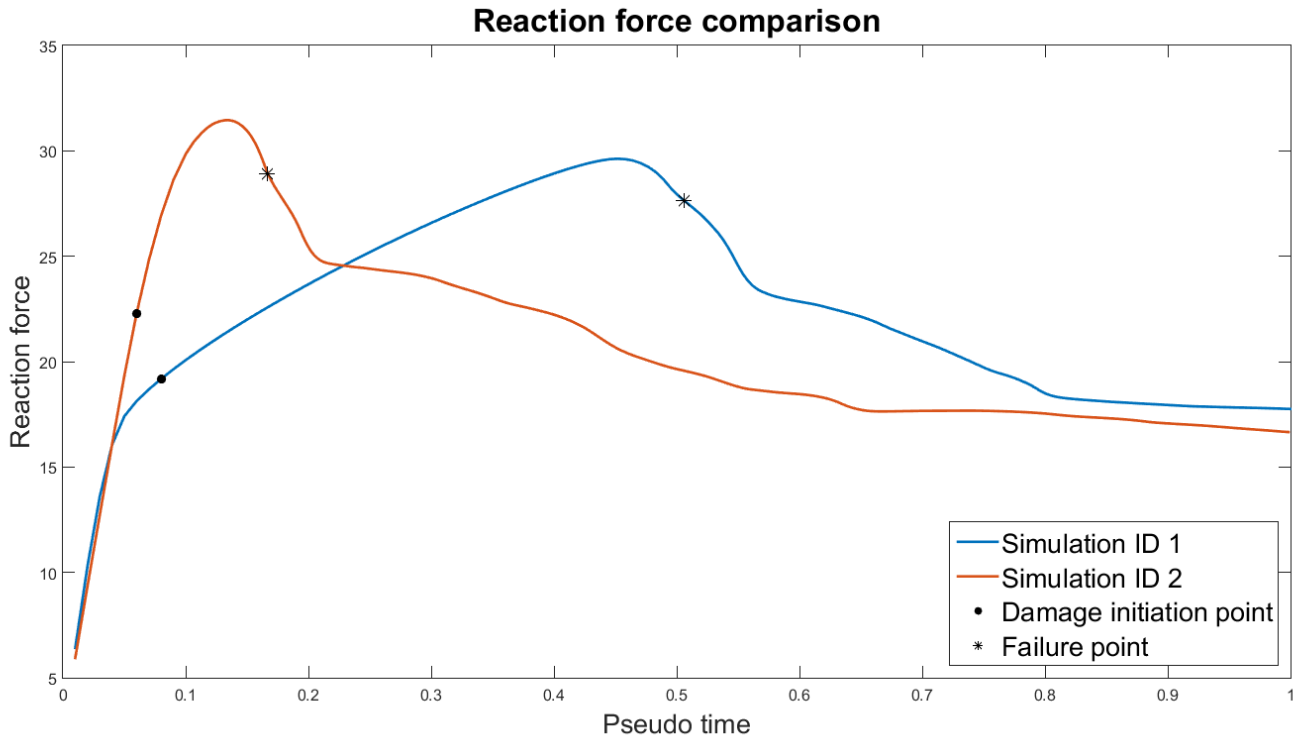

Figure 19 Reaction force graph comparison of simulation set I

Simulation set II compares the different microstructure morphology: number of grains in x direction is gradually changed. Figure 20, 20, 21, 22 illustrate the resultant intergranular fracture. Figure 25 shows that with increasing number of grains the system becomes softer. An assumption here is that it happens because more cohesive zone elements are introduced in the system, so they have bigger impact on the overall response of the

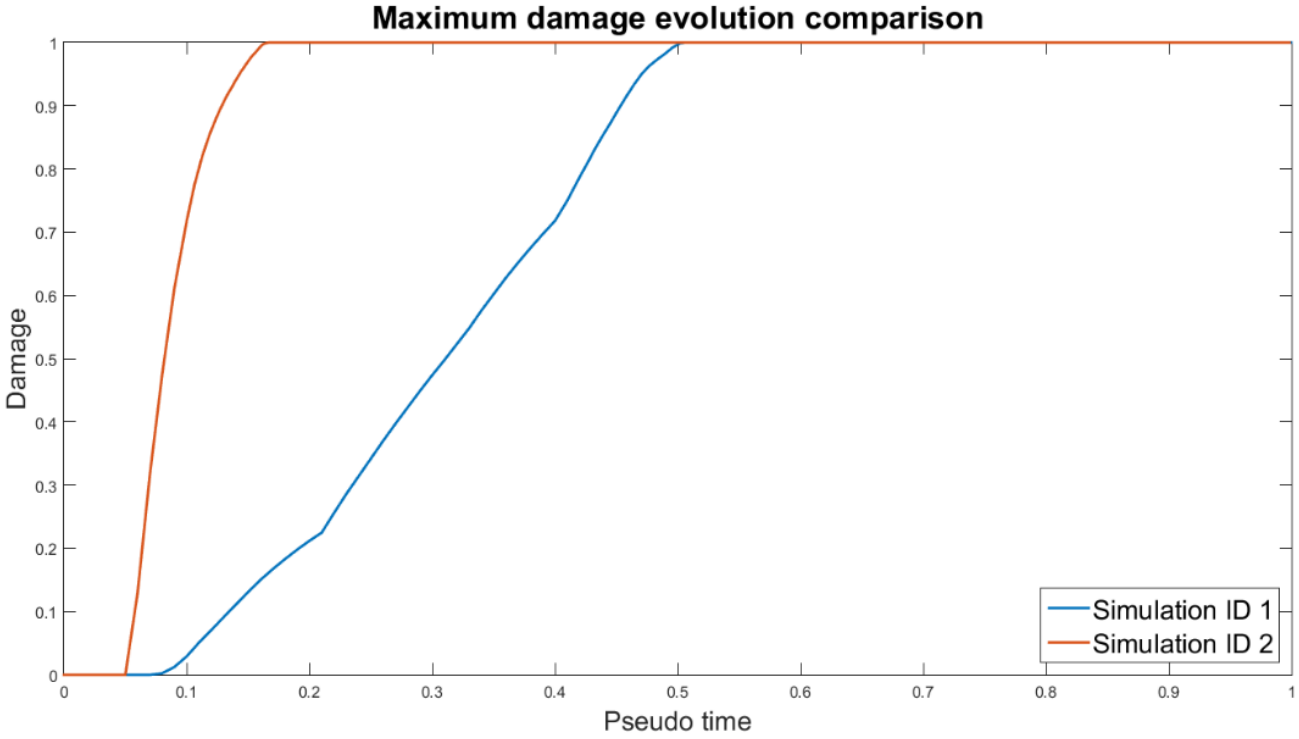

Figure 18 Maximum damage graph comparison of simulation set I

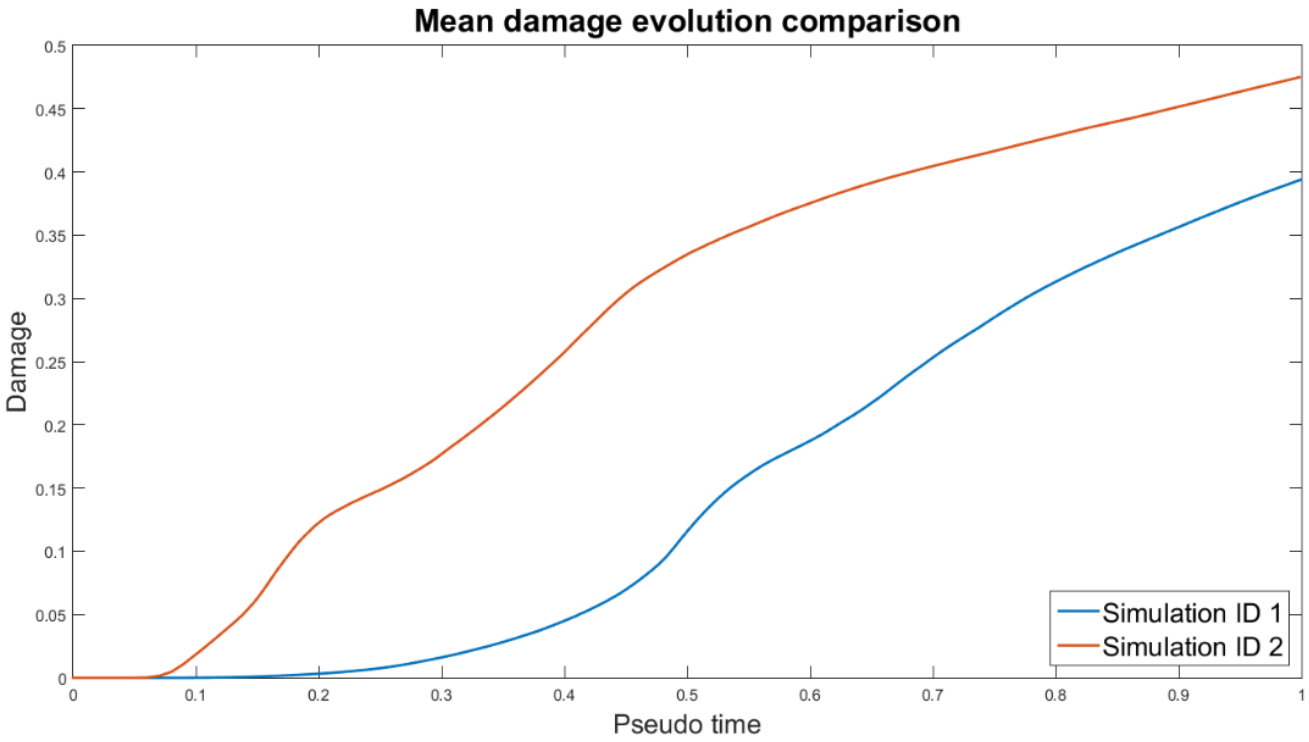

Figure 21 Mean damage graph comparison of simulation set I

system. According to Figure 26 time between first crack initiation and first interface failure increases with increasing number of grains, but the Simulation ID 6 deviates from this trend and shows more brittle behavior. Overall, mean damage in the system is decreasing with increasing number of grains (Figure 27).

Generally, the simulation of the tensile test gives the similar crack propagation behavior to the experiment of the tensile test (Figure 28).

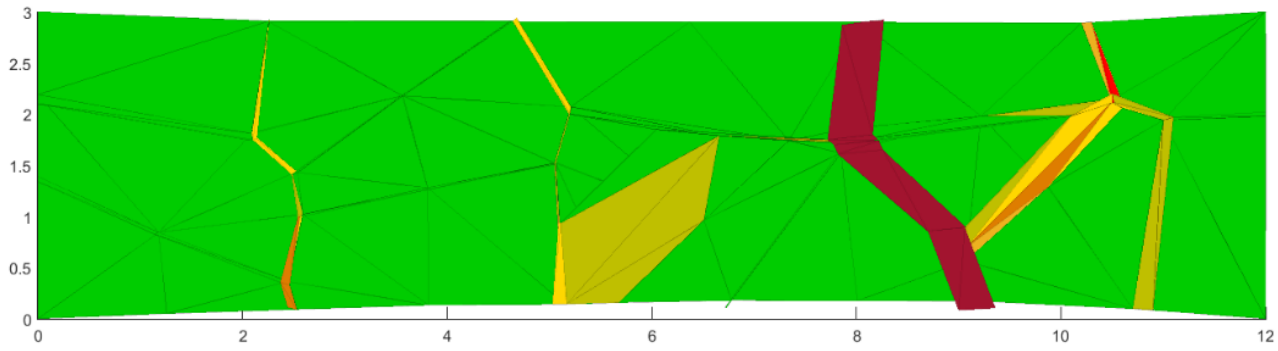

Figure 20 Top view of cohesive zone damage. Simulation ID 3

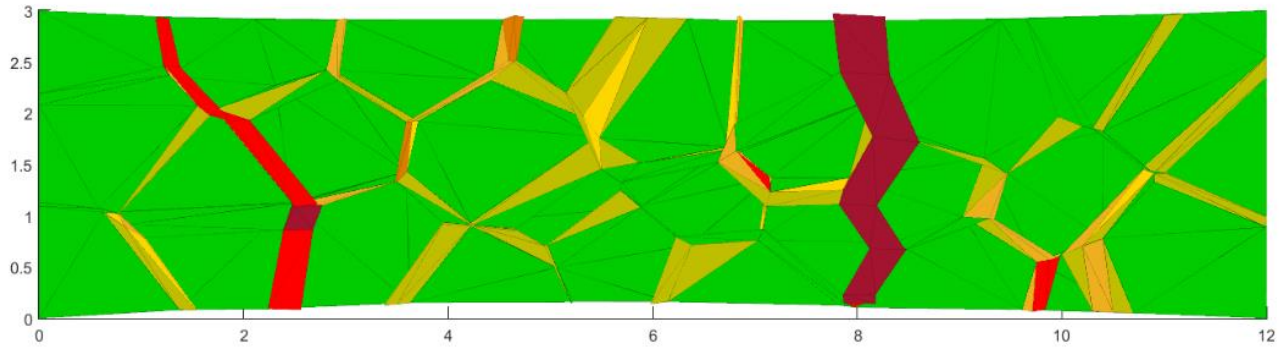

Figure 22 Top view of cohesive zone damage. Simulation ID 4

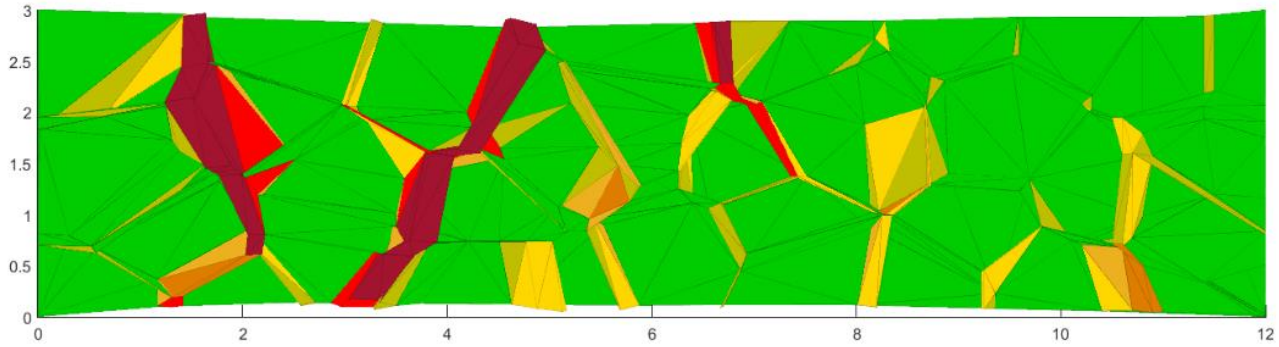

Figure 23 Top view of cohesive zone damage. Simulation ID 5

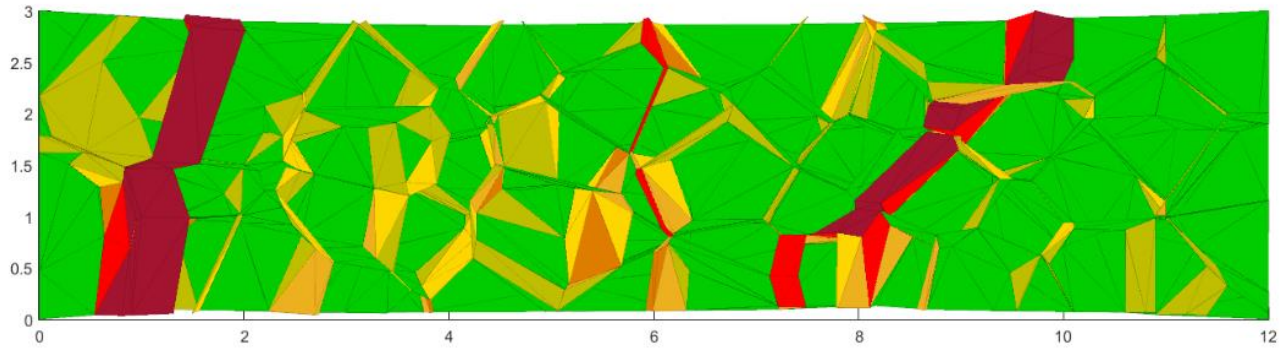

Figure 24 Top view of zohesive zone damage. Simulation ID 6

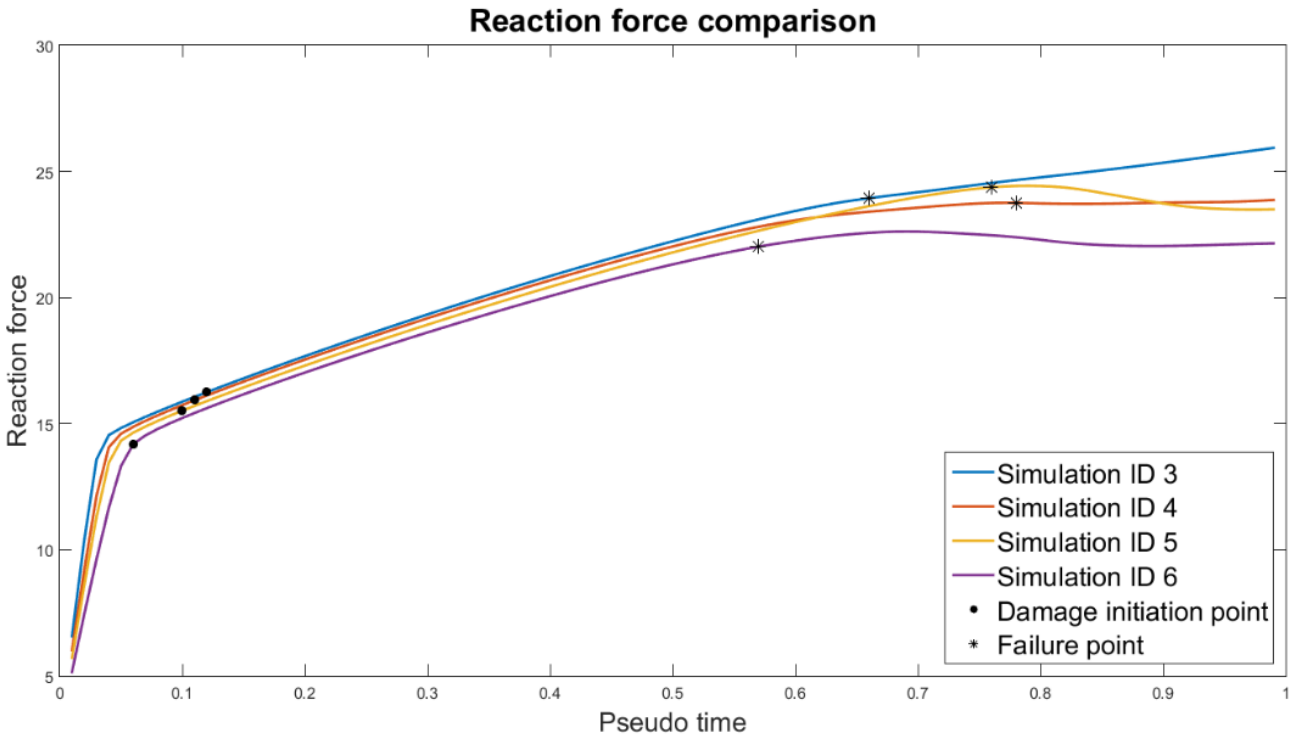

Figure 25 Reaction force graph comparison of simulation set II

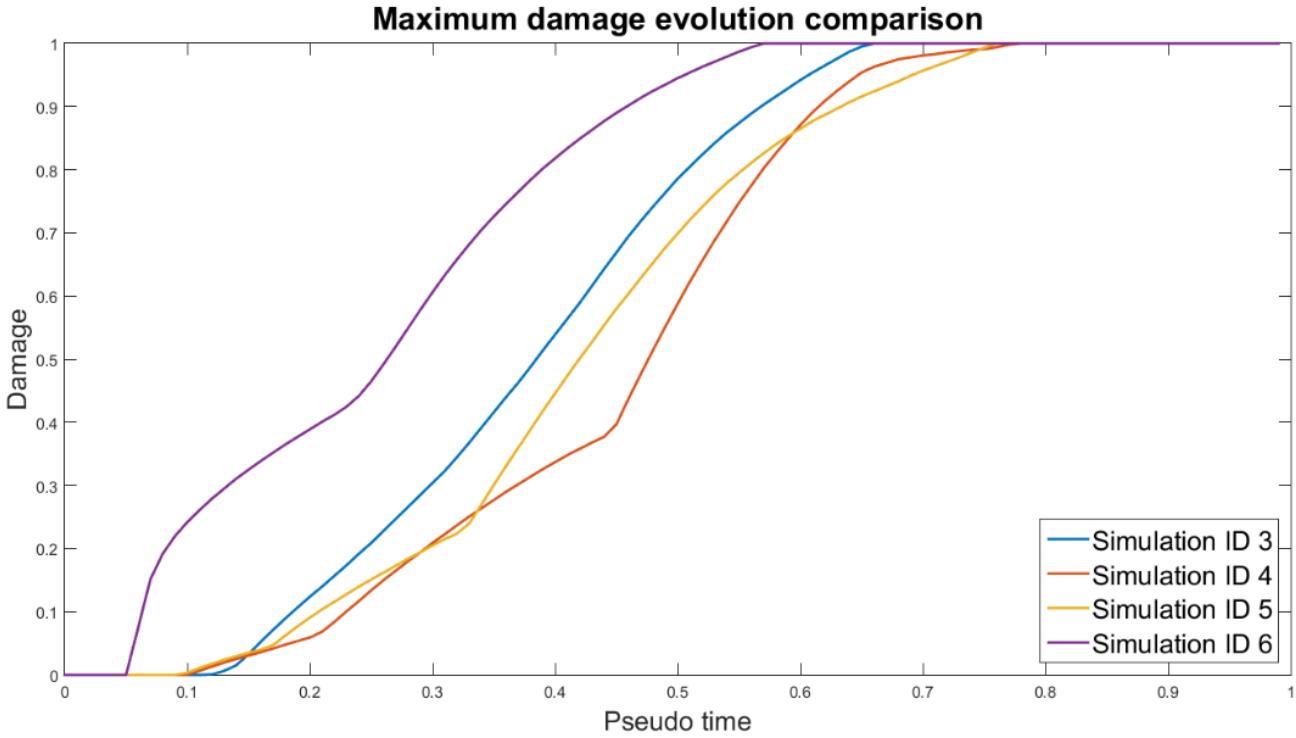

Figure 26 Maximum damage graph comparison of simulation set II

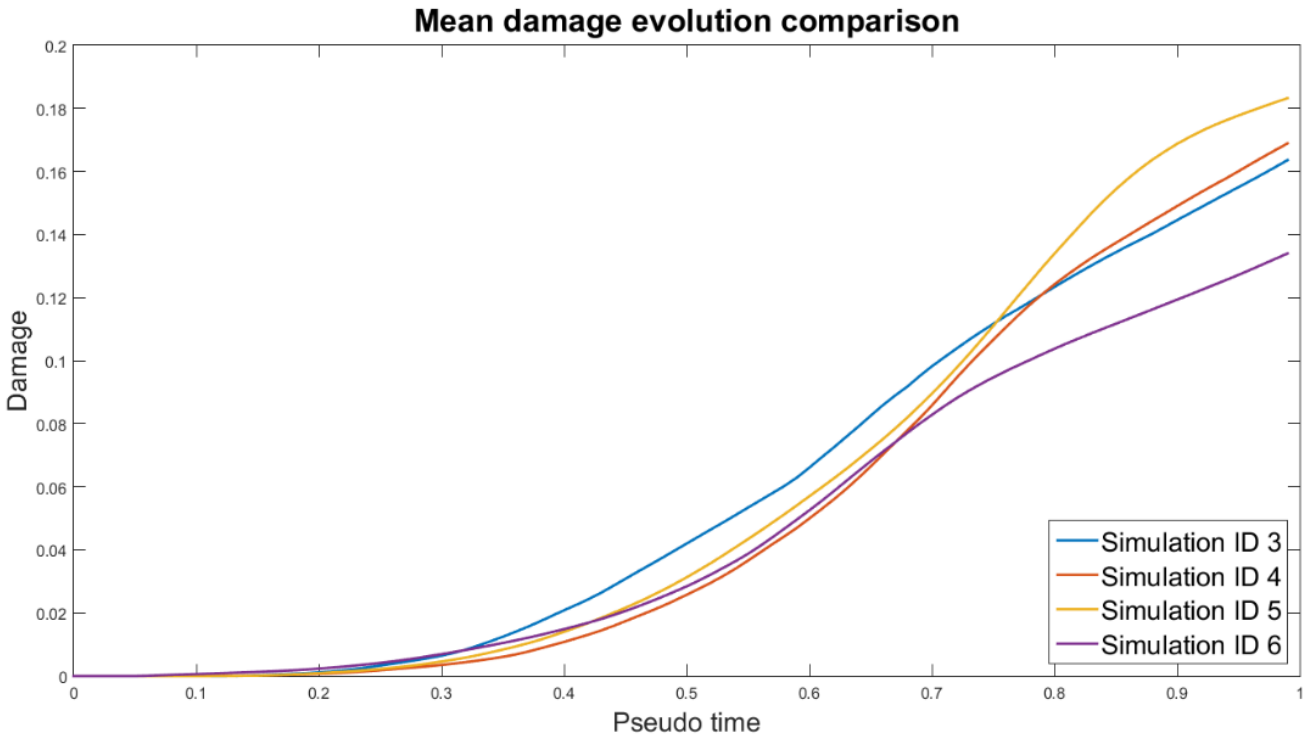

Figure 27 Mean damage graph comparison of simulation set II

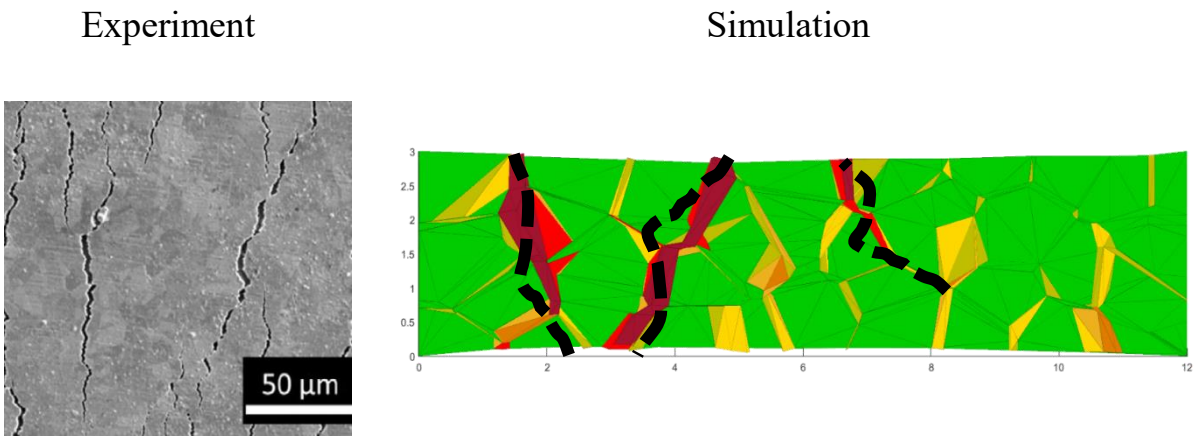

Figure 28 Top view of the experiment and simulation results of the tensile test

6.2 Nanoindentation test results

Figure 29, 27, 28, 29 show the resultant intergranular damage inside the coating. It is seen that the crack starts to grow in the indentator impact zone and grows in the outward radial directions. Figure 33 shows that the system becomes harder with decreasing the number of grains. Time between crack initiation and first interface failure is increasing with decreasing the number of grains (Figure 34). Mean damage in the system is increasing with decreasing the number of grains (Figure 35).

The Simulation ID 9 and the Simulation ID 10 were compared to study the effect of increasing number of layers in the system. Figure 36 shows the same trend as for other simulations that with increasing number of grains the system becomes softer and mean damage in the system is lower for the geometry with two layers of grains (Figure 39). The difference in this case that the time between the crack initiation and first interface failure also increases.

The results of the nanoindentation test simulations show similar crack propagation to the experiments (Figure 38).

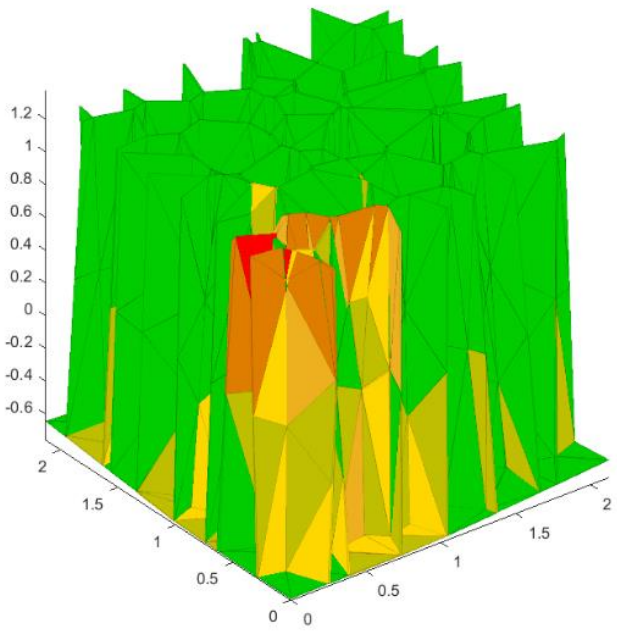

Figure 29 Isometric view of cohesive zone damage. Simulation ID 7

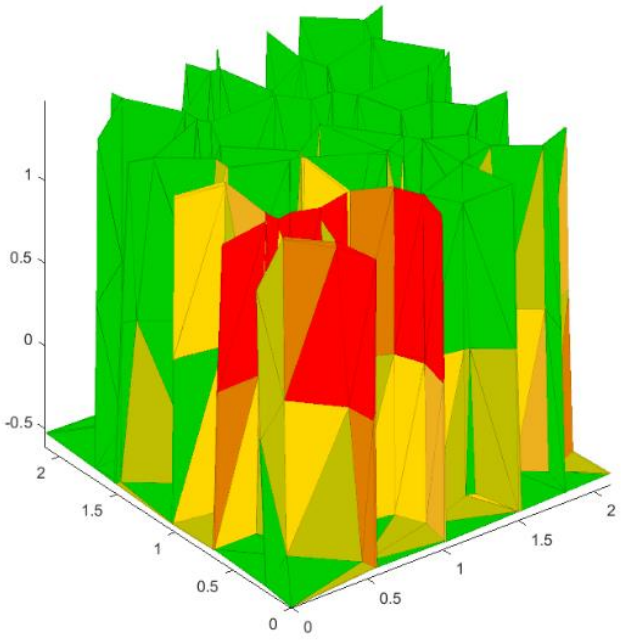

Figure 30 Isometric view of cohesive zone damage. Simulation ID 8

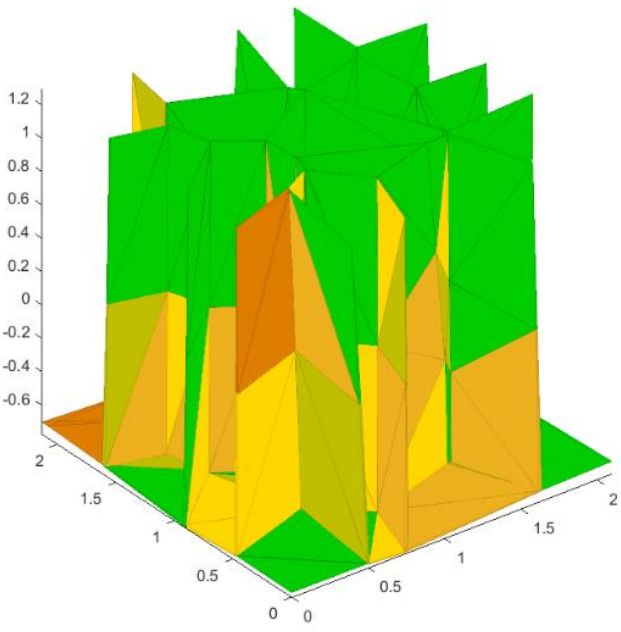

Figure 31 Isometric view of cohesive zone damage. Simulation ID 9

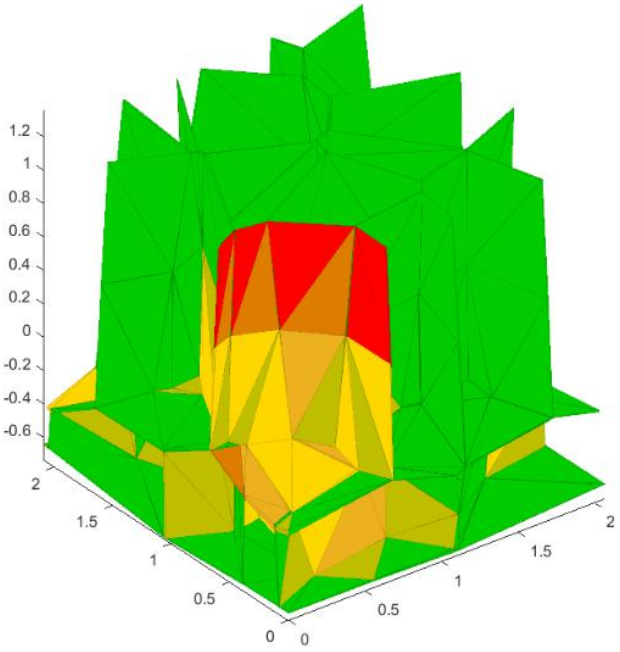

Figure 32 Isometric view of cohesive zone damage. Simulation ID 10

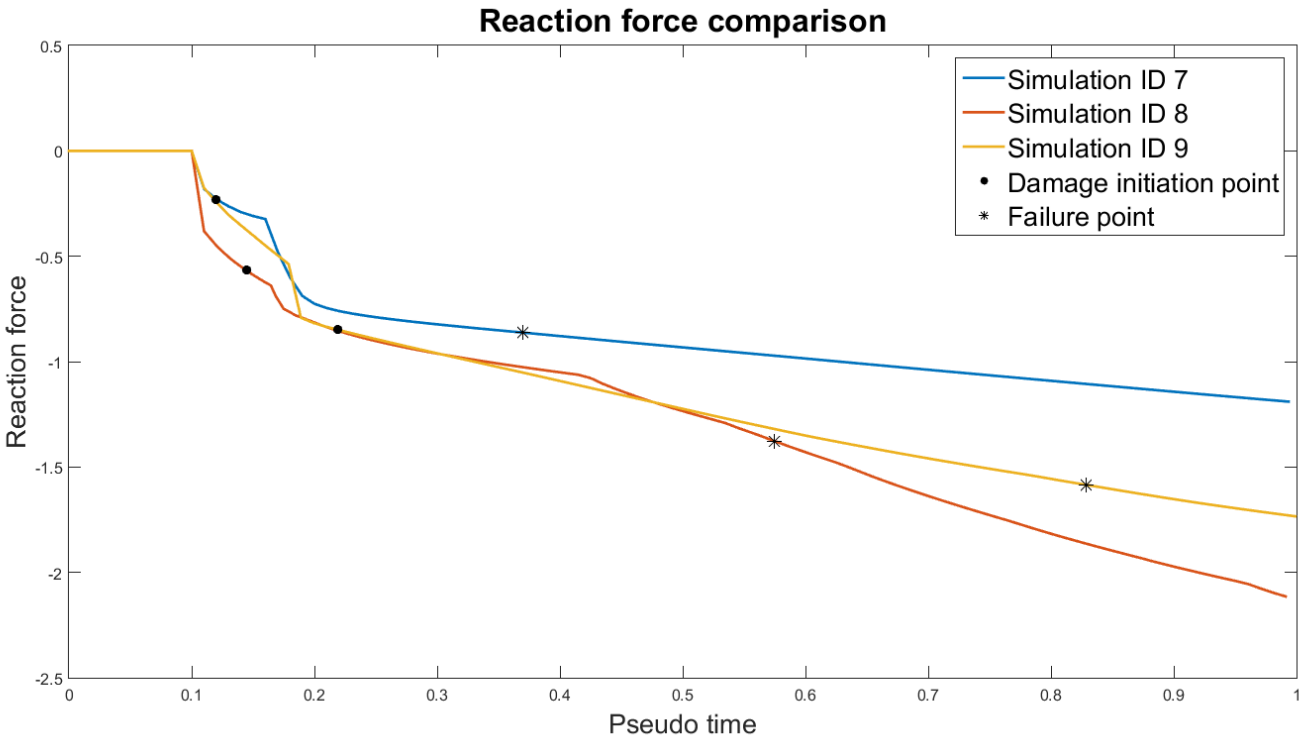

Figure 33 Reaction force comparison graph of changing number of grains

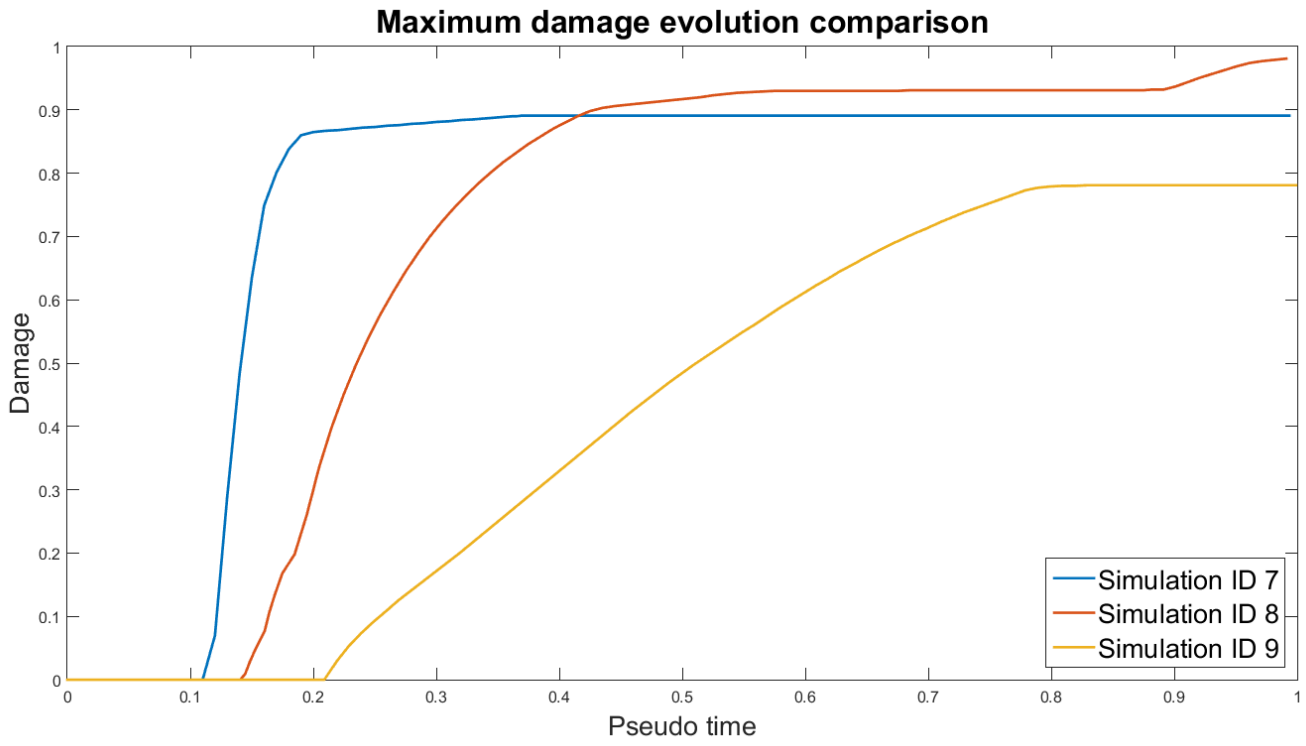

Figure 34 Maximum damage comparison graph of changing number of grains

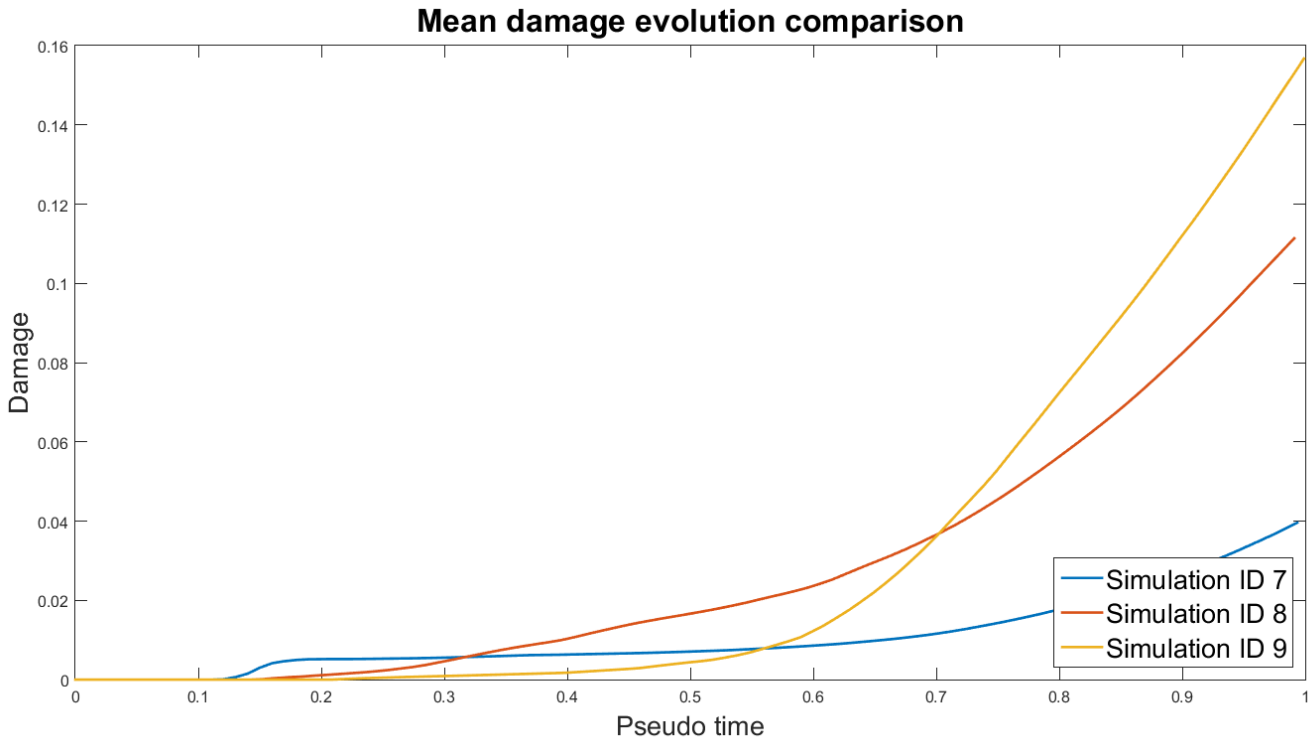

Figure 35 Mean damage comparison graph of changing number of grains

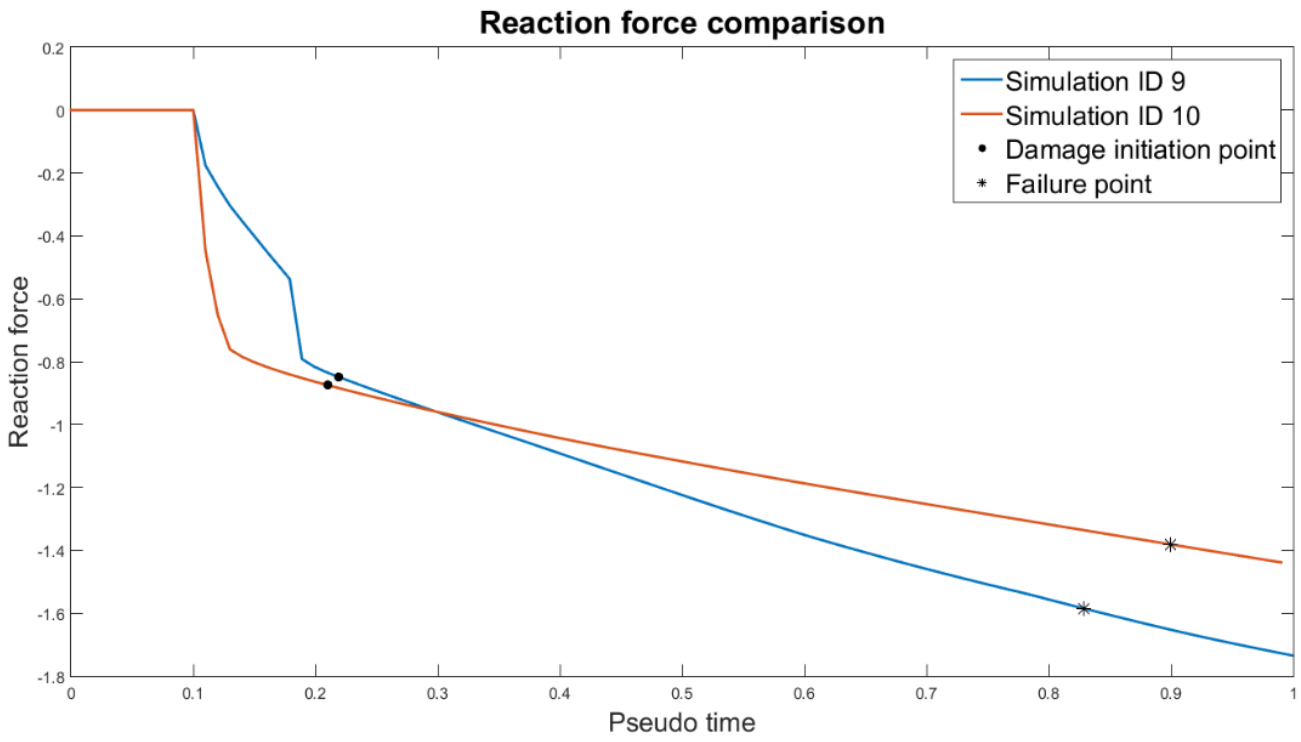

Figure 36 Reaction force comparison graph of changing number of layers

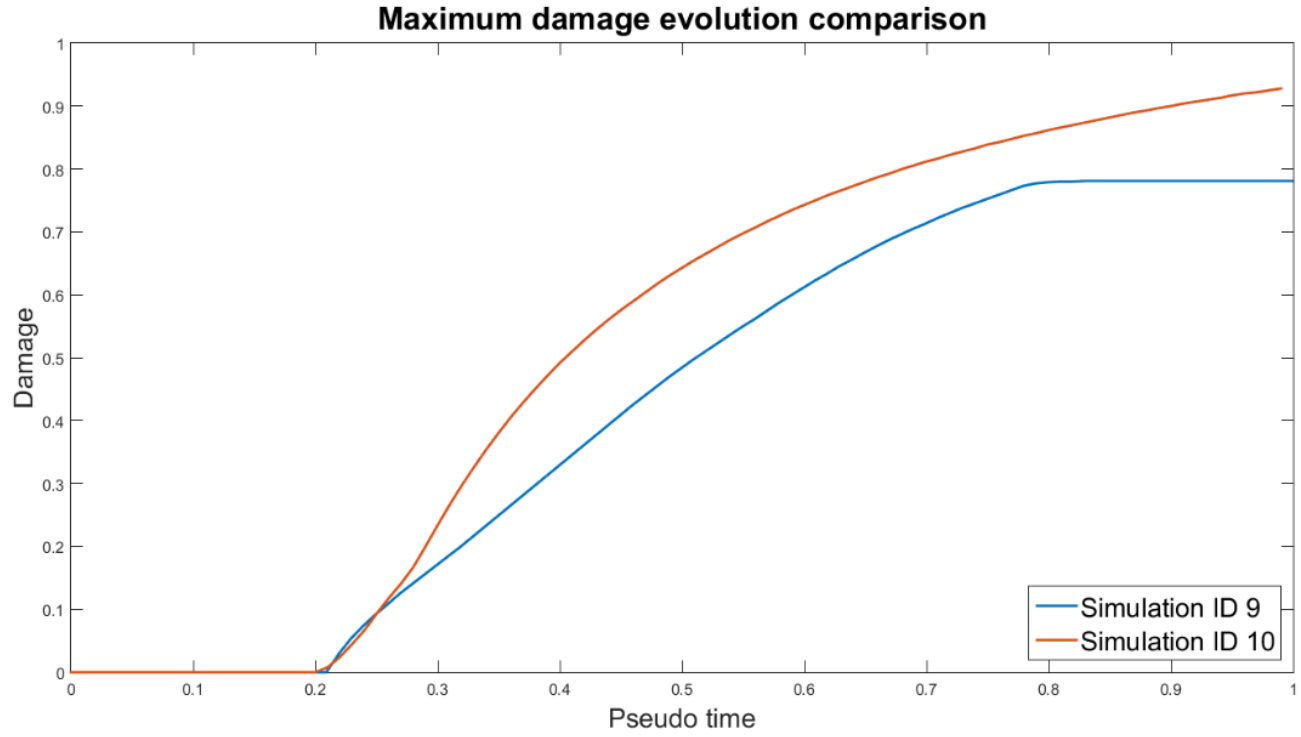

Figure 37 Maximum damage comparison graph of changing number of layers

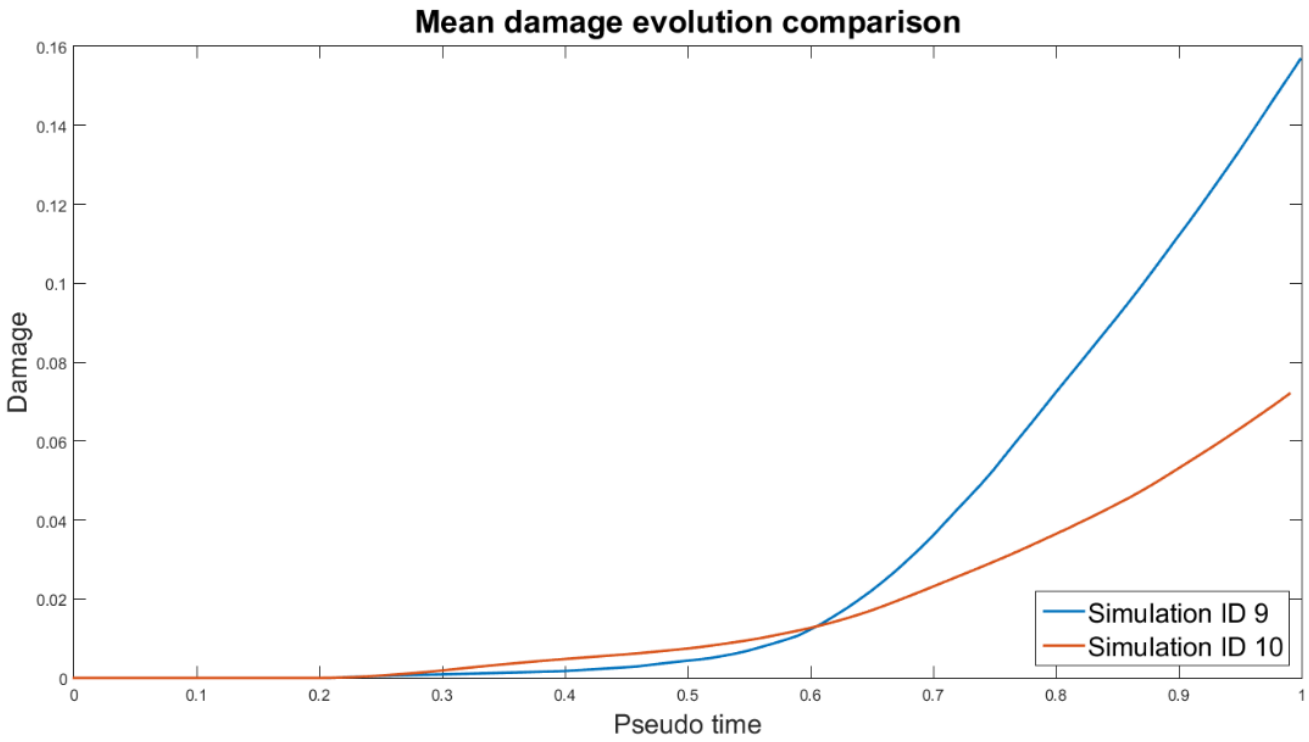

Figure 39 Mean damage comparison graph of changing number of layers

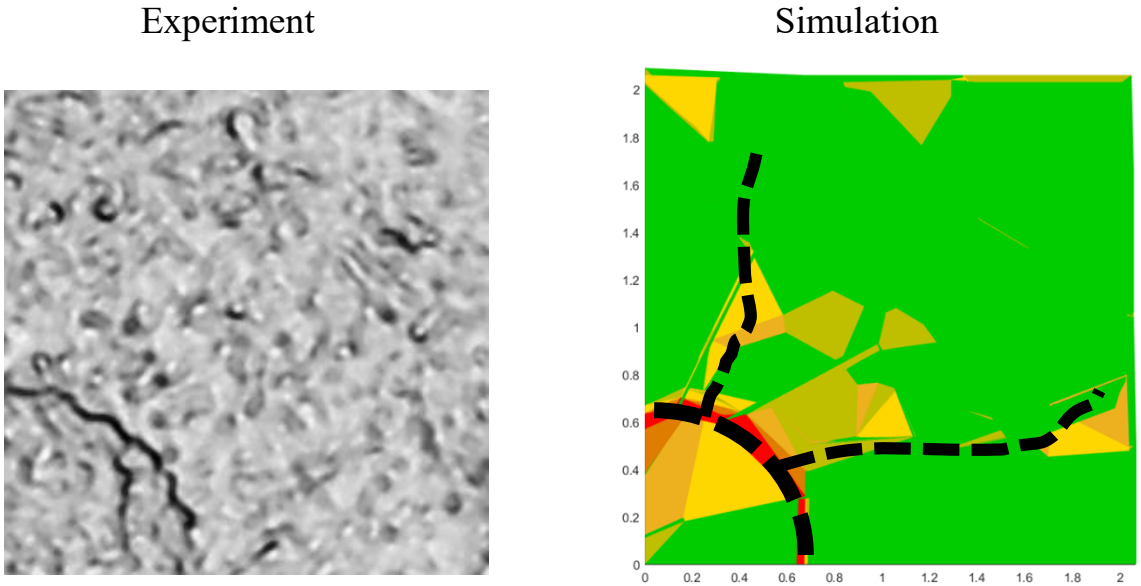

Figure 38 Top view of the experiment and simulation results of the nanoindentation test

7 CONCLUSIONS

The goal of this thesis was to model the geometry of coating microstructure and to include grain boundary mechanisms to the system. The MATLAB script was created to generate the microstructure model using the Voronoi diagram. The generated models were meshed with an open source software Gmsh. The grain interface interaction behavior was modelled with cohesive zone elements, which were inserted into the mesh with the developed MATLAB script.

Finite element simulations were performed using the Finite Element Analysis Program (FEAP). Two different test cases, a tensile test and a nanoindentation test, were used in the analysis to verify the generated coating-substrate system model.

The results showed that using cohesive zone elements at the grain boundaries gives us the possibility to model the behavior of intergranular crack propagation. The relation between changing grain number and damage was observed here. The relation there was that with an increasing number of grains the first interface failure happened faster, but overall mean damage in the system was observed to diminish. This means that an increasing number of grains results in an increased overall resistance to damage.

The results showed that it is possible to vary the morphology of a microstructure and predict the damage in the coating. The simulated crack propagation had a similar behavior as in real-life experiments. The developed scripts can be used to obtain quantitatively accurate results of the coating microstructure response under loads, but detailed experimental results for the calibration of the solid material and grain interface behavior are needed.

In this thesis, the number of grains in the model was relatively low; in order to achieve precise results a model with a significantly higher number of grains should be used. However, with an increasing number of grains in the model, the number of finite elements will increase, and the computation time will increase significantly. Therefore, a finite element solver which is capable of parallel computing should be used in further developments.

BIBLIOGRAPHY

Barenblatt, G.I., 1962. The Mathematical Theory of Equilibrium Cracks in Brittle Fracture. *Advances in Applied Mechanics*, 7, pp.55-129.

Beckmann, F., Grupp, R., Haibel, A., Huppmann, M., Nöthe, M., Pyzalla, A., Reimers, W., Schreyer, A. & Zettler, R., 2007. In-Situ Synchrotron X-Ray Microtomography Studies of Microstructure and Damage Evolution in Engineering Materials. *Advanced Engineering Materials*, 9(11), pp.939-50.

Berg, M.d., Cheong, O., Kreveld, M.v. & Overmars, M., 2008. *Computational Geometry Algorithms and Applications*. 3rd ed. Berlin: Springer.

Bobzin, K., Brögelmann, T., Brugnara, R.H., Arghavani, M., Yang, T.-S., Chang, Y.-Y. & Chang, S.-Y., 2015. Investigation on plastic behavior of HPPMS CrN, AlN and CrN/AlN-multilayer coatings using finite element simulation and nanoindentation. *Surface & Coatings Technology*, 284, pp.310-17.

Brenner, S.C. & Scott, L.R., 2008. *The Mathematical Theory of Finite Element Methods*. 3rd ed. New York: Springer.

Camacho, G.T. & Ortiz, M., 1996. Computational modeling of impact damage in brittle materials. *International Journal of Solids and Structures*, 33(20-22), pp.2899-938.

Descartes, R., 1644. *Principia Philosophiae*. Amsterdam: Ludovicus Elzevirius.

Geubelle, P.H. & Baylor, J., 1998. Impact-induced delamination of laminated composites: a 2D simulation. *Composites Part B: Engineering*, 29(5), pp.589-602.

Geuzaine, C. & Remacle, J.-F., 2016. *Gmsh 2.12*. [Online] Available at: http://gmsh.info/doc/texinfo/gmsh.html [Accessed 26 March 2016].

Hughes, T.J.R., 1987. *The Finite Element Method Linear Static and Dynamic Finite Element Analysis*. New Jersey: Prentice-Hall, Inc.

Kheradmand, N., Barnoush, A. & Vehof, H., 2010. Investigation of the role of grain boundary on the mechanical properties of metals. *Journal of Physics: Conference Series*, 240(1).

Lejcek, P., 2010. *Grain Boundary Segregation in Metals*. Berlin: Springer Berlin Heidelberg.

MathWorks, 2016. *Delaunay Triangulation*. [Online] Available at: mathworks.com/help/matlab/math/delaunay-triangulation.html [Accessed 26 March 2016].

MathWorks, 2016. *MATLAB*. [Online] Available at: mathworks.com/products/matlab/ [Accessed 30 April 2016].

Needleman, A., 1990. An analysis of tensile decohesion along an interface. *Journal of the Mechanics and Physics of Solids*, 38(3), pp.289-324.

Okabe, A., Boots, B., Sugihara, K. & Chiu, S.n., 2000. *Spatial tessellations: Concepts and Applications of Voronoi Diagrams*. 2nd ed. Chichester: John Wiley & Sons, Ltd.

Paggi, M. & Wriggers, P., 2011. A nonlocal cohesive zone model for finite thickness interfaces – Part II: FE. *Computational Materials Science*, 50(5), pp.1634-43.

Poon, B., Rittel, D. & Ravichandran, G., 2008. An analysis of nanoindentation in linearly elastic solids. *International Journal of Solids and Structures*, 45(24), pp.6018–33.

Salvo, L., Suéry, M., Marmottant, A., Limodin, N. & Bernard, D., 2010. 3D imaging in material science: Application of X-ray tomography. *Comptes Rendus Physique*, (11), pp.641-49.

Sarakinos, K., Alami, J. & Konstantinidis, S., 2010. High power pulsed magnetron sputtering: A review on scientific and engineering. *Surface & Coatings Technology*, 204(11), pp.1661–84.

Schwartzman, S., 1996. *The Words of Mathematics: An Etymological Dictionary of Mathematical Terms Used in English*. Washington: The Mathematical Association of America.

Sfantos, G.K. & Aliabadi, M.H., 2007. A boundary cohesive grain element formulation for modelling intergranular microfracture in polycrystalline brittle materials. *Numerical Methods for Engineering*, 69(8), pp.1590-626.

Simonovski, I. & Cizelj, L., 2015. Cohesive zone modeling of intergranular cracking in polycrystalline aggregates. *Nuclear Engineering and Design*, 283, pp.139-47.

Taylor, R.L., 2015. *FEAP*. [Online] Available at: ce.berkeley.edu/projects/feap/ [Accessed 30 April 2016].

Tvergaard, V. & Hutchinson, J.W., 1992. The relation between crack growth resistance and fracture process parameters in elastic–plastic solids. *Journal of the Mechanics and Physics of Solids*, 40(6), pp.1377-97.

Voronoy, G., 1908. Nouvelles applications des paramètres continus à la théorie de formes quadratiques. *Journal für die reine und angewandte Mathematik*, 134, pp.198-287.